

SYNTHESIS AND FABRICATION OF CARBON NANOTUBE BASED
COMPOSITE MATERIALS
FOR FUEL CELL CATALYST AND ULTRA-RESILIENT AEROGEL

A Dissertation

by

WOONGCHUL CHOI

Submitted to the Office of Graduate and Professional Studies of
Texas A&M University
in partial fulfillment of the requirements for the degree of

DOCTOR OF PHILOSOPHY

Chair of Committee,	Choongho Yu
Committee Members,	Miladin Radovic
	Mohammad Naraghi
	Partha Mukherjee
Head of Department,	Ibrahim Karaman

August 2017

Major Subject: Materials Science and Engineering

Copyright 2017 Woongchul Choi

ABSTRACT

Carbon nanotubes have been actively investigated in a wide range of applications since carbon nanotubes have excellent electrical, thermal, and mechanical properties. In particular, a great deal of research is being carried out to improve and control their properties by different functionalization methods. Among them, I have developed two functionalization methods for the controlling of properties, which are doping carbon nanotubes with heteroatoms and fabricating polymer composite based on carbon nanotubes.

I studied a facile one-step synthesis method of nitrogen-iron coordinated carbon nanotube catalysts without precious metals. Our catalyst shows excellent onset ORR potential comparable to those of other precious metal free catalysts, and the maximum limiting current density from our catalysts is larger than that of the Pt-based catalysts.

In addition to the development of carbon nanotubes-based aerogel composite, I studied the facile and quick process for the scalable production of super resilient CNT-PDMS composite by microwave heating with ultra-low thermal conductivity and high electrical properties. This report describes that the microwave heating process can lead to a quick reaction and allow for the uniform polymer layer on CNT, which enhance the mechanical properties of carbon nanotube composite. Furthermore, CNT-PDMS composite aerogel shows high mechanical strength (0.18 MPa), compressibility, thermal insulation ($26 \text{ mW m}^{-1} \text{ K}^{-1}$) and elasticity-dependent electric conduction.

DEDICATION

This dissertation is dedicated to my beloved and supportive family, for their endless encouragement, unconditional trust, and true love.

ACKNOWLEDGEMENTS

First, I would like to sincerely thank my supervisor, Dr. Choongho Yu, for his patient guidance, support, advice and inspiration to my research throughout my Ph.D. course. Dr. Yu's enthusiasm and commitment to the research is what I need to carry on in my future career. I also truly appreciate the help and suggestions from my committee members, Dr. Miladin Radovic, Dr. Mohammad Naraghi, and Dr. Partha Mukherjee.

Also, I appreciate the members of Nano Energy Lab for their friendship and support.

I would like to present my deep gratitude to my family, for their numerous supports and sacrifices. Words cannot express how grateful I am for the love and trust they have shown me.

CONTRIBUTORS AND FUNDING SOURCES

Contributors

This work was supervised by a dissertation committee consisting of Professor Choongho Yu(advisor), Miladin Radovic, and Mohammad Naraghi of the Department of Materials Science and Engineering and Professor Partha Mukherjee of the Department of Mechanical Engineering.

The thermal gravimetric analysis (TGA) for Chapter 2 was provided by Professor Hung-Jue Sue. The Transmission electron microscopy (TEM) analyses depicted in Chapter 2 and 3 were conducted in part by Gang Yang of the Department of Mechanical Engineering.

All other work conducted for the dissertation was completed by the student, under the advisement of Professor Choongho Yu of the Department of Mechanical Engineering.

Funding Sources

This work was made possible in part by US National Science Foundation under Grant Number (CMMI 1030958).

TABLE OF CONTENTS

	Page
ABSTRACT	ii
DEDICATION	iii
ACKNOWLEDGEMENTS	iv
CONTRIBUTORS AND FUNDING SOURCES.....	v
TABLE OF CONTENTS	vi
LIST OF FIGURES.....	viii
LIST OF TABLES	xii
CHAPTER I INTRODUCTION AND LITERATURE REVIEW	1
1.1 Introduction	1
1.1.1 Historical introduction of carbon materials.....	1
1.1.2 Basic background of carbon nanotubes.....	4
1.1.3 The doping of carbon nanotubes	9
1.1.4 Carbon nanotubes polymer composites.....	9
1.2 Nitrogen-doped graphitic carbon for non-precious metal catalysts	11
1.2.1 Fuel cell cathode: main drawback	11
1.2.2 Precious metal catalyst: major cost driver of electrochemical cells.....	15
1.2.3 Transition metal catalysts for oxygen reduction	17
1.2.4 Nitrogen-doped graphitic carbon structures for substituting precious metal catalysts	19
1.3 Carbon nanotubes polymer composite by microwave heating.....	21
1.3.1 Carbon nanotubes polymer composite aerogel	21
1.3.2 The advantages of microwave heating	22
CHAPTER II ONE-STEP SYNTHESIS OF NITROGEN-IRON COORDINATED CARBON NANOTUBE CATALYSTS FOR OXYGEN REDUCTION REACTION.....	27

2.1 Introduction	27
2.2 Experimental section	29
2.2.1 Synthesis and characterization	29
2.2.2 Electrochemical measurements	31
2.3 Results and Discussion	33
2.3.1 Morphology and material structure	33
2.3.2 Electrochemical analysis	35
2.4 Conclusions	44
CHAPTER III ULTRA-RESILIENT CARBON NANOTUBE COMPOSITES AEROGEL WITH THERMAL INSULATION AND ELECTRICAL PROPERTIES BY MICROWAVE IRRADIATION.....	45
3.1 Introduction	45
3.2 Experimental section	48
3.2.1 Carbon nanotube sponge synthesis	48
3.2.2 Carbon nanotube - PDMS composite fabrication	48
3.2.3 Characterization	49
3.2.4 Mechanical properties characterization.....	50
3.2.5 Electrical properties and thermal conductivity measurement	50
3.3 Results and discussion	51
3.3.1 Fabrication and structural features of nanocomposites	51
3.3.2 Characterization of composite aerogel structure	56
3.3.3 Mechanical properties of CNT-PDMS composite aerogel.....	58
3.3.4 Thermal insulation and electric properties of CNT-PDMS composite aerogel	61
3.4 Conclusions	68
CHAPTER IV SUMMARY AND CONCLUSIONS.....	69
4.1 One-step synthesis of nitrogen-iron coordinated carbon nanotube catalysts for oxygen reduction reaction	69
4.2 Ultra-resilient carbon nanotube composites aerogel with thermal insulation and electrical properties by microwave irradiation	70
REFERENCES	72

LIST OF FIGURES

	Page
Figure 1 The observation of multi-wall carbon nanotubes by HRTEM with various inner and outer diameter, d_i and d_o , and number of cylindrical wall, N . (a) $N = 5$, $d_o = 67 \text{ \AA}$ (b) $N = 2$, $d_o = 55 \text{ \AA}$ (c) $N = 7$, $d_o = 67 \text{ \AA}$, and $d_i = 23 \text{ \AA}$ (reprinted with permission from [9]).	2
Figure 2 (a) The chiral vector OA or $C_h = n\hat{a}_1 + m\hat{a}_2$ is demonstrated on the honeycomb lattice of carbon atoms by unit vectors \hat{a}_1 and \hat{a}_2 and the chiral angle θ in terms of the zigzag axis. (b) Possible vectors indicated by the pairs of integers (n, m) for general carbon nanotubes, including zigzag, armchair, and chiral nanotubes. (reprinted with permission from [9])	5
Figure 3 Schematic of single wall carbon nanotubes with the nanotubes axis normal to the chiral vector: (a) the $\theta = 30^\circ$ direction (b) the $\theta = 0^\circ$ direction (c) a general θ direction with $0 < \theta < 30^\circ$. (reprinted with permission from [9]).	6
Figure 4 Operation and structure of a polymer electrolyte fuel cell (PEFC). (reprinted with permission from [32])	12
Figure 5 Manufacturing costs of major components in PEM fuel cells. The high electrode cost is mainly due to the high price of platinum catalysts.	16
Figure 6 Schematic explanation of oxygen adsorption on a transition metal (a), and oxygen reduction by transferring electrons from the metal electrode to oxygen (b). (reprinted with permission from [47]).	17
Figure 7 Fe(II)phthalocyanine, (a where Fe is surrounded by nitrogen and aromatic carbons. (reprinted with permission from [47]).	18
Figure 8 Schematic of heat introduction for conventional heating and microwave heating.....	25
Figure 9 The SEM and TEM images of Fe-A/P-CNT (a)~(c), Fe-A-CNT (d), Fe-P-CNT (e), P-A-CNT (f), and Fe-CNT (g).	34

Figure 10 Raman spectra of the iron-incorporated CNTs and the intensity ratio of D-band to G-band (I_D/I_G).....	35
Figure 11 (a) RDE polarization curves of Fe-CNT, A/P-CNT, Fe-P-CNT, Fe-A-CNT, Fe-A/P-CNT, and Pt/C in O_2 -saturated 0.1 M KOH electrolyte with 1600 rpm and 5 mV s^{-1} , respectively. (b) CV results of Fe-A/P-CNT, Fe-P-CNT, and Fe-A-CNT in N_2 - and O_2 -saturated 0.1 M KOH electrolyte with a scan rate of 100 mV s^{-1} . (c) CV results of Fe-CNT, A/P-CNT and Pt/C in O_2 -saturated 0.1 M KOH electrolyte with a scan rate of 100 mV s^{-1}	37
Figure 12 (a) Survey XPS scan results of Fe-A/P-CNT, Fe-A-CNT, and Fe-P-CNT. (b) The comparison of iron atomic concentration of doped carbon nanotubes.	39
Figure 13 (a) TGA results of Fe-P-CNT, Fe-A-CNT, and Fe-A/P-CNT. (b) XRD result of Fe-A/P-CNT	40
Figure 14 (a) N-1s XPS results of Fe-A/P-CNT, Fe-A-CNT and Fe-P-CNT. The vertical broken lines indicate the peak location of pyridinic nitrogen. (b) Fe-2p XPS results of Fe-A/P-CNT, Fe-A-CNT and Fe-P-CNT. The vertical broken lines indicate peak location of surface Fe^{3+}	41
Figure 15 (a) RDE polarization curves of Fe-A/P-CNT in O_2 -saturated 0.1 M KOH electrolyte at 6 different rotational speeds of the electrode, starting from 1600 rpm to 850 rpm (every 150 rpm). (b) The Koutecky-Levich plots for Fe-A/P-CNT from the RDE results. (c) The RDE polarization curves of Fe-A/P-CNT were compared with those of commercial Pt/C before and after 10000, 20000, and 30000 CV cycles. The rotating speed and the scan rate were 1600 rpm and 5 mV s^{-1} , respectively.	43
Figure 16 The microwave heating effect for polar and nonpolar materials. (a) DI water, (b) Hexane, and (c) PDMS. The photographs show the temperature different between before microwave and after microwave. The images indicate hexane and PDMS didn't absorb microwaves.....	52
Figure 17 The curing PDMS polymer on carbon nanotubes sponge. (a) Photograph shows the PDMS solution drops onto CNT. (b) SEM image of pristine CNT sponge (c-f) SEM images of CNT-PDMS nanocomposite after microwave irradiation.	53

Figure 18	Fabrication and microstructure of CNT-PDMS composite aerogel. (a) Schematic of synthesis steps for making CNT-PDMS composite aerogel (b,c) SEM image of a 0.5 vol% PDMS nanocomposite sponge structure (d,e) TEM images of a 0.5 vol% PDMS composite aerogel structure, showing the structure of nanocomposite which has a very thin PDMS layer on the graphitic wall of carbon nanotubes.	55
Figure 19	The SEM images of CNT-PDMS composite aerogel with different PDMS contents. (a) 3.2 vol% (b) 8 vol%.	55
Figure 20	Characterization of CNT-PDMS composite aerogel structure. (a) Infrared spectra of CNT sponge, PDMS, and 0.5 vol% PDMS composite aerogel. (b) Raman spectra of CNT sponge and 0.5 vol% PDMS composite aerogel.	57
Figure 21	Compressive mechanical property of CNT-PDMS composite aerogel (a) Compressive stress-strain curves of CNT-PDMS composite aerogel at different set strains of 30, 60, and 80%, respectively. (b) Maximum compressive stress of CNT-PDMS composite aerogel and pristine CNT sponge at 60% strain. The black and grey bars represent the first and 200 th cycle during compressive test.	58
Figure 22	Mechanical properties of CNT-PDMS composite aerogel. (a) The photographs of the CNT-PDMS composite sponge at the different strains in the first compression cycle. (b) Compressive stress history of CNT-PDMS composite aerogel for 8,000 cycles at 60% compressive strain. (c) Maximum compressive stress of CNT-PDMS composite aerogel and pristine CNT sponge for 8,000 cycles at 60% strain. (d) Comparison of the compressive mechanical stability of CNT-PDMS composite aerogel and other materials. Note that the relative compressive stress of other materials would be different with different densities and we chose the best performance value from literatures.	59
Figure 23	Thermal insulation and electric properties of CNT-PDMS composite aerogel. (a) Thermal conductivity values of pristine CNT sponge, CNT-PDMS composite aerogel, and after 1,000 cyclic compressive test with 60% strain. (b) Thermal conductivity values and porosity of CNT-PDMS composite aerogel with different PDMS contents. (c) R/R_0 of the CNT-PDMS composite aerogel when repeatedly compressed ($\epsilon=50\%$) for 100 cycles.	62

Figure 24 Pore size distribution of CNT-PDMS composite aerogel.....	64
Figure 25 R/R_0 of the CNT-PDMS composite aerogel as a function of compressive strain ($\epsilon=60\%$).....	66

LIST OF TABLES

	Page
Table 1 Structural configurations for carbon nanotubes (reprinted with permission from [9]).	8
Table 2 List of catalysts and corresponding precursors used for synthesis. The samples were grown on quartz plates except A/P-CNT, which was grown from Fe (6 nm)/Al (10 nm) deposited Si wafers.	31
Table 3 TGA and XPS analysis of Fe-P-CNT, Fe-A-CNT, and Fe-A/P-CNT.	38
Table 4 Estimation of gas and solid thermal conductivity of nanocomposite aerogel.....	65
Table 5 Comparison of the materials properties of CNT-PDMS nanocomposite and other materials.....	67

CHAPTER I

INTRODUCTION AND LITERATURE REVIEW

1.1 Introduction

Carbon nanotubes have been actively investigated in a wide range of applications since carbon nanotubes have excellent electrical, thermal, and mechanical properties[1-3]. The recent literature shows that the investigation of properties and applications of pristine carbon nanotubes has extremely developed. In particular, a great deal of research is being carried out to improve and control their properties by different functionalization methods[3, 4]. Among them, I have developed two functionalization methods for the controlling of properties, which are doping carbon nanotubes with heteroatoms and fabricating polymer composite based on carbon nanotubes. This chapter describes the introduction of the carbon nanotubes, the doping of carbon nanotubes, and the polymer composites, which can be utilized to control the properties of carbon nanotubes for several applications.

1.1.1 Historical introduction of carbon materials

In the 1970's and 1980's, small diameter (< 10 nm) carbon filaments were made by the synthesis of vapor grown carbon fibers using the decomposition of hydrocarbons at high temperatures in the presence of transition metal catalyst particles[5-7]. However,

they didn't report the detailed systematic studies of thin carbon filaments in these early years, and it was not called carbon nanotubes before the observation of carbon nanotubes by *Iijima* using high-resolution transmission electron microscopy(HRTEM) in 1991, as shown in figure 1[8].

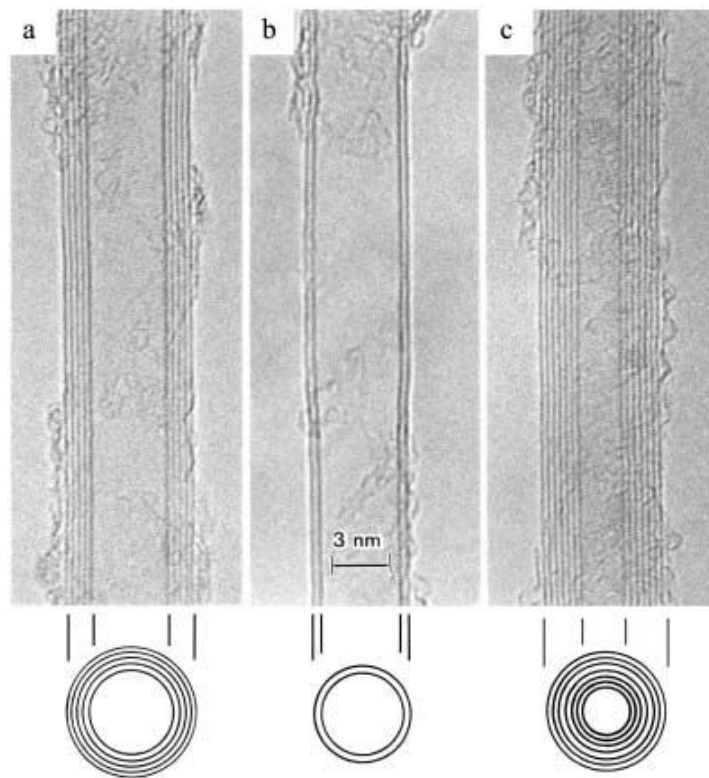


Figure 1. The observation of multi-wall carbon nanotubes by HRTEM with various inner and outer diameter, d_i and d_o , and number of cylindrical wall, N . (a) $N = 5$, $d_o = 67 \text{ \AA}$ (b) $N = 2$, $d_o = 55 \text{ \AA}$ (c) $N = 7$, $d_o = 67 \text{ \AA}$, and $d_i = 23 \text{ \AA}$ (reprinted with permission from [9])

The systematic study of carbon filaments resulted from the discovery of fullerene by *Kroto, Smalley, Curl*, and coworkers at Rice university[10]. Actually, Smalley and others speculated that a single wall carbon nanotube might be a case of a fullerene molecule[9]. The connection between carbon nanotubes and fullerenes was further studied by the investigation that the end of carbon nanotubes was fullerene-like caps. It is interesting that the smallest diameter of carbon nanotube is same as the diameter of the C_{60} molecule, indicating the smallest fullerene to follow the isolated pentagon rule. This rule needs that no two pentagons are next to one another, for this reason, lowering the strain energy of the fullerene cage. Based on these studies and the *Iijima's* observation, carbon nanotubes research has been done. The initial investigation was for multi-wall nanotubes, it was experimentally discovered by *Iijima* group and *Bethune*[11, 12]. These results were particularly important since the single wall carbon nanotubes are fundamental structure and had been the origin for the theoretical studies. The most important of theoretical research was the prediction that carbon nanotubes could be either semiconducting or metallic properties in accordance with geometrical characteristics, such as the diameter of carbon nanotubes and the orientation of their hexagons with regard to the carbon nanotubes axis[13-15]. Although they reported these results in 1992, it was not clear before 1998 that these theoretical studies were verified experimentally[16, 17].

Smalley and coworkers at Rice university successfully synthesized the aligned single wall carbon nanotube with a small diameter, therefore, utilizing it to conduct

many experiment with regard to 1D quantum physics which was not previously conducted[18]. Absolutely, actual carbon nanotubes have finite length, defects, and interact with other nanotubes or the substrate, causing complicated their behavior.

1.1.2 Basic background of carbon nanotubes

The structure of carbon nanotubes has been investigated by high resolution transmission electron microscopy (HRTEM) and scanning tunneling microscopy (STM)[19], resulting in straight confirmation that the carbon nanotubes are seamless cylinders originated from the honeycomb lattice on behalf of a single atomic layer of graphite, called a graphene sheet, as shown in figure 2a. The structure of a single wall carbon nanotubes is clearly described in respect of 1D unit cell, describing the vectors C_h and T , as shown in figure 2a.

The circumference of carbon nanotube is demonstrated in respect of the chiral vector $C_h = n\hat{a}_1 + m\hat{a}_2$ which links two crystallographically equivalent sites on a graphene sheet (figure 2a)[13]. The structure (figure 2a) depends on the pair of integers (n, m) which indicate the chiral vector. Figure 2a displays the chiral angle (θ) between the chiral vector, the “zigzag” direction ($\theta = 0$), and the unit vectors \hat{a}_1 and \hat{a}_2 of the graphene sheet.

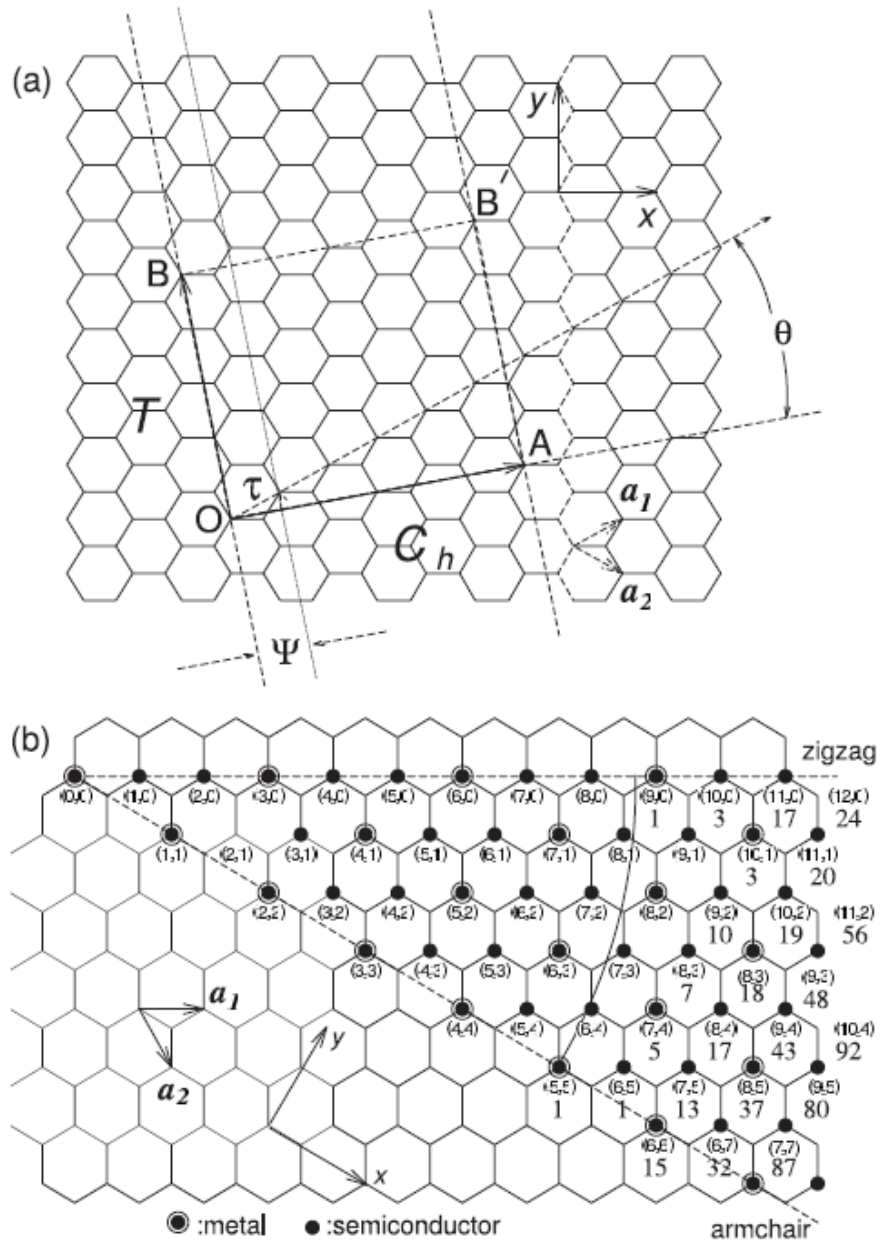


Figure 2. (a) The chiral vector $\vec{O}A$ or $\vec{C}_h = n\hat{a}_1 + m\hat{a}_2$ is demonstrated on the honeycomb lattice of carbon atoms by unit vectors \hat{a}_1 and \hat{a}_2 and the chiral angle θ in terms of the zigzag axis. (b) Possible vectors indicated by the pairs of integers (n, m) for general carbon nanotubes, including zigzag, armchair, and chiral nanotubes (reprinted with permission from [9])

Three distinct types of carbon nanotube structures can be produced by rolling up the graphene sheet into a cylinder as shown in figure 3. The zigzag and armchair nanotubes match to chiral angles of $\theta = 0,30^\circ$, and $0 < \theta < 30^\circ$.

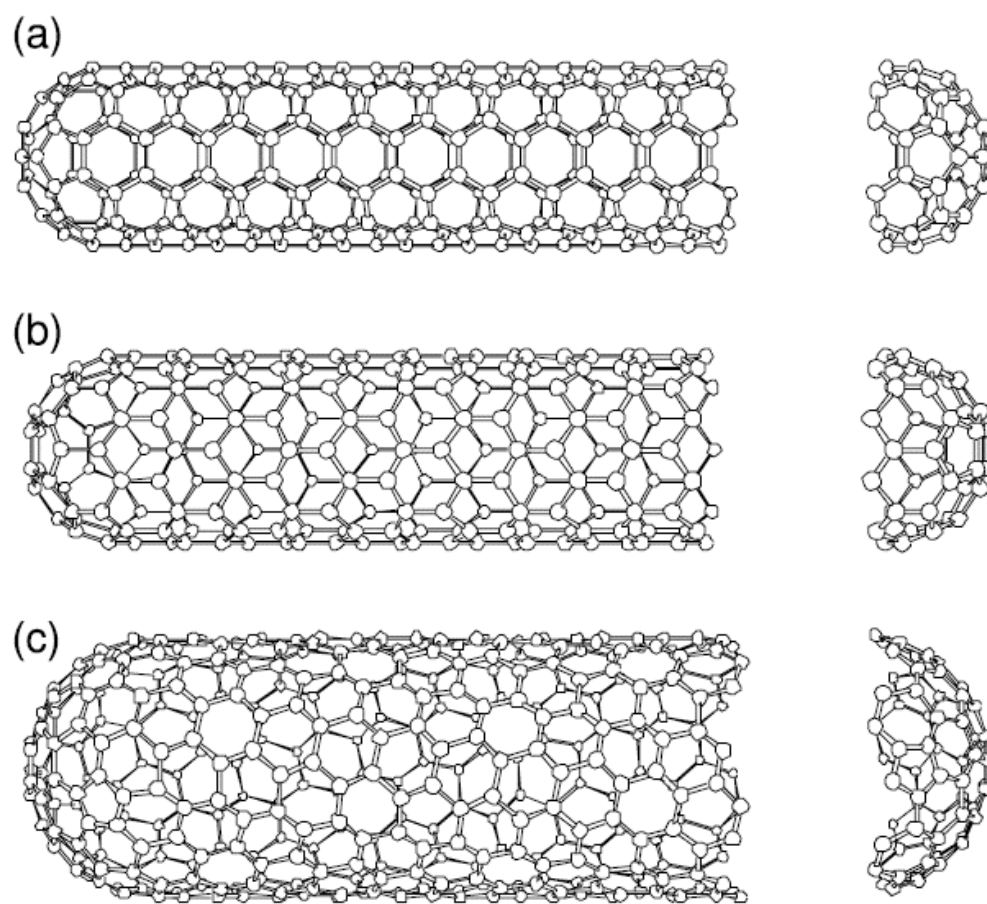


Figure 3. Schematic of single wall carbon nanotubes with the nanotubes axis normal to the chiral vector: (a) the $\theta = 30^\circ$ direction (b) the $\theta=0^\circ$ direction (c) a general θ direction with $0<\theta<30^\circ$ (reprinted with permission from [9])

The cylinder connecting the two hemispherical caps of carbon nanotubes, as shown in figure 3, is created by superimposing the two ends of the vectors and the cylinder connection is made along the two lines, \overrightarrow{OB} and $\overrightarrow{AB'}$, in figure 2a. In the (n, m) notation for $C_h = n\hat{a}_1 + m\hat{a}_2$, the vectors $(n, 0)$ or $(0, m)$ mean zigzag nanotubes and the vectors (n, n) indicates armchair nanotubes. All other vectors (n, m) accord with chiral nanotubes[9]. The diameter d_t of nanotubes is given by

$$d_t = \sqrt{3}a_{C-C}(m^2 + mn + n^2)^{1/2}\pi^{-1} = C_h/\pi \quad (1)$$

where C_h is the length of C_h and a_{C-C} is the C-C bond length. The chiral angle θ is given by

$$\theta = \tan^{-1}[\sqrt{3}n/(2m + n)] \quad (2)$$

From (2), it follows that the $\theta = 30^\circ$ for (n, n) armchair carbon nanotubes and that the $(n, 0)$ zigzag carbon nanotubes. Armchair and zigzag nanotubes have a mirror plane and therefore are regarded as achiral. Difference in the carbon nanotube diameter and chiral angle can bring about the differences in the properties of the carbon nanotubes. In addition, the number of hexagons, N , per unit cell of a chiral nanotubes is given by

$$N = 2(m^2 + n^2 + nm)/d_R \quad (3)$$

where $d_R=d$ (if $n-m$ is not a multiple of $3d$) or $d_R=3d$ (if $n-m$ is a multiple of $3d$). A hexagon in the honeycomb lattice has two carbon atoms. The unit cell area of carbon nanotubes is N times larger than that for a graphene layer, thereby the unit cell area for carbon nanotubes in reciprocal space is correspondingly $1/N$ times smaller. Table 1

shows a summary of relations useful for describing the structure of single wall carbon nanotubes[9, 20].

Table 1. Structural configurations for carbon nanotubes (reprinted with permission from [9])

symbol	name	formula	value
a	length of unit vector	$a = \sqrt{3}a_{C-C} = 2.49 \text{ \AA}$,	$a_{C-C} = 1.44 \text{ \AA}$
$\hat{\mathbf{a}}_1, \hat{\mathbf{a}}_2$	unit vectors	$\left(\frac{\sqrt{3}}{2}, \frac{1}{2}\right)a, \left(\frac{\sqrt{3}}{2}, -\frac{1}{2}\right)a$	x, y coordinate
$\hat{\mathbf{b}}_1, \hat{\mathbf{b}}_2$	reciprocal lattice vectors	$\left(\frac{1}{\sqrt{3}}, 1\right)\frac{2\pi}{a}, \left(\frac{1}{\sqrt{3}}, -1\right)\frac{2\pi}{a}$	x, y coordinate
\mathbf{C}_h	chiral vector	$\mathbf{C}_h = n\hat{\mathbf{a}}_1 + m\hat{\mathbf{a}}_2 \equiv (n, m),$	$(0 \leq m \leq n)$
L	length of \mathbf{C}_h	$L = \mathbf{C}_h = a\sqrt{n^2 + m^2 + nm}$	
d_t	diameter	$d_t = L/\pi$	
θ	chiral angle	$\sin \theta = \frac{\sqrt{3}m}{2\sqrt{n^2 + m^2 + nm}}$	$0 \leq \theta \leq \frac{\pi}{6}$
		$\cos \theta = \frac{2n + m}{2\sqrt{n^2 + m^2 + nm}},$	$\tan \theta = \frac{\sqrt{3}m}{2n + m}$
d	$\text{gcd}(n, m)^b$		
d_R	$\text{gcd}(2n + m, 2m + n)^b$	$d_R = \begin{cases} d & \text{if } (n - m) \text{ is not multiple of } 3d \\ 3d & \text{if } (n - m) \text{ is multiple of } 3d \end{cases}$	
\mathbf{T}	translational vector	$\mathbf{T} = t_1\hat{\mathbf{a}}_1 + t_2\hat{\mathbf{a}}_2 \equiv (t_1, t_2)$	$\text{gcd}(t_1, t_2) = 1^b$
		$t_1 = \frac{2m + n}{d_R}, t_2 = -\frac{2n + m}{d_R}$	
T	length of \mathbf{T}	$T = \mathbf{T} = \frac{\sqrt{3}L}{d_R}$	
N	Number of hexagons in the nanotube unit cell.	$N = \frac{2(n^2 + m^2 + nm)}{d_R}$	
\mathbf{R}	symmetry vector	$\mathbf{R} = p\hat{\mathbf{a}}_1 + q\hat{\mathbf{a}}_2 \equiv (p, q)$	$\text{gcd}(p, q) = 1^b$
		$t_1q - t_2p = 1,$ $(0 < mp - nq \leq N)$	
τ	pitch of \mathbf{R}	$\tau = \frac{(mp - nq)T}{N} = \frac{MT}{N}$	
ψ	rotation angle of \mathbf{R}	$\psi = \frac{2\pi}{N}$	in radians
M	number of \mathbf{T} in $N\mathbf{R}$.	$N\mathbf{R} = \mathbf{C}_h + M\mathbf{T}$	

1.1.3 The doping of carbon nanotubes

The pristine carbon nanotubes possess excellent electrical properties depending on their structure, such as diameter and chirality[21, 22]. However, carbon nanotubes can be intentionally tuned their electrical properties by introducing heteroatoms or molecules since the electrical properties of carbon nanotubes are strongly connected to the delocalized electron system[23]. This phenomenon is called doping. The doping carbon nanotubes has been actively studied since it allows to tailor their electronic properties.

There are three different ways of doping carbon nanotubes, intercalation, encapsulation, and substitutional doping. In particular, substitutional doping within carbon nanotubes has been enormously studied since substitutional doping can introduce highly localized electronic properties in the valence or conduction bands[24]. For example, nitrogen doping can improve the electrical properties of carbon nanotubes, resulting in the enhancement of cross correlation between carbon and guest molecules due to nitrogen have one additional electron compared to carbon[25, 26].

1.1.4 Carbon nanotubes polymer composites

The excellent mechanical properties of carbon nanotubes are promising the enhancement of mechanical properties in polymer composites[27]. The enhancement of mechanical properties in carbon nanotubes polymer composites can be described by the rule of mixture [28].

$$E_c = V_f E_f + (1 - V_f) E_m \quad (4)$$

where E_c , E_m and E_f are Young's modulus of the composite, carbon nanotubes fiber and polymer matrix, respectively. According to the rule of mixture, only small volume of carbon nanotubes is needed to enhance polymer composite since Young's modulus of carbon nanotubes is around 1TPa[29].

Polymer reinforced carbon nanotubes composite also enhance their flexibility and elasticity[30]. Since the elasticity is one of the most important properties of aerogel materials, the hybridization with polymer is a useful method for the reinforcement of mechanical property of aerogel Polymer provides flexible bridging connected to carbon nanotubes and acts as spacers and flexible link in carbon nanotubes network in aerogel, which induce polymer composite aerogel to rubber elasticity behavior.

1.2 Nitrogen-doped graphitic carbon for non-precious metal catalysts

1.2.1 Fuel cell cathode: main drawback

Electrochemical cells are promising future renewable energy systems with broad ranges of applications. For example, PEM fuel cells belong to a group of electrochemical cell systems that generate electricity without producing greenhouse gases. Fuel cells owing to their high-energy efficiency, environmental friendliness and minimal noise are perceived to play a key role in the present scenario of a global quest towards a clean and sustainable energy future. The hydrogen-air polymer electrolyte fuel cell (PEFC) shown in figure 4 is arguably the frontrunner in the hydrogen economy and fuel cell race. Notwithstanding the excellent perspectives of hydrogen economy and electrochemical energy conversion, the demands on material and process optimization in PEFCs in terms of sustained performance under widely varying operating conditions, lifespan, and materials costs in view of commercialization are formidable. Despite tremendous recent progress, a pivotal performance limitation in PEFCs centers on the cathode catalyst layer owing to sluggish kinetics of the oxygen reduction reaction (ORR) and several transport losses. Platinum and Pt-based electrocatalysts, commonly used in the PEFC electrodes, not only contribute to high fuel cell cost but also lead to durability concerns in terms of Pt cathode oxidation, catalyst migration, loss of electrode active surface area, and corrosion of the carbon support.

Hydrogen Oxidation Reaction (HOR) Oxygen Reduction reaction (ORR)

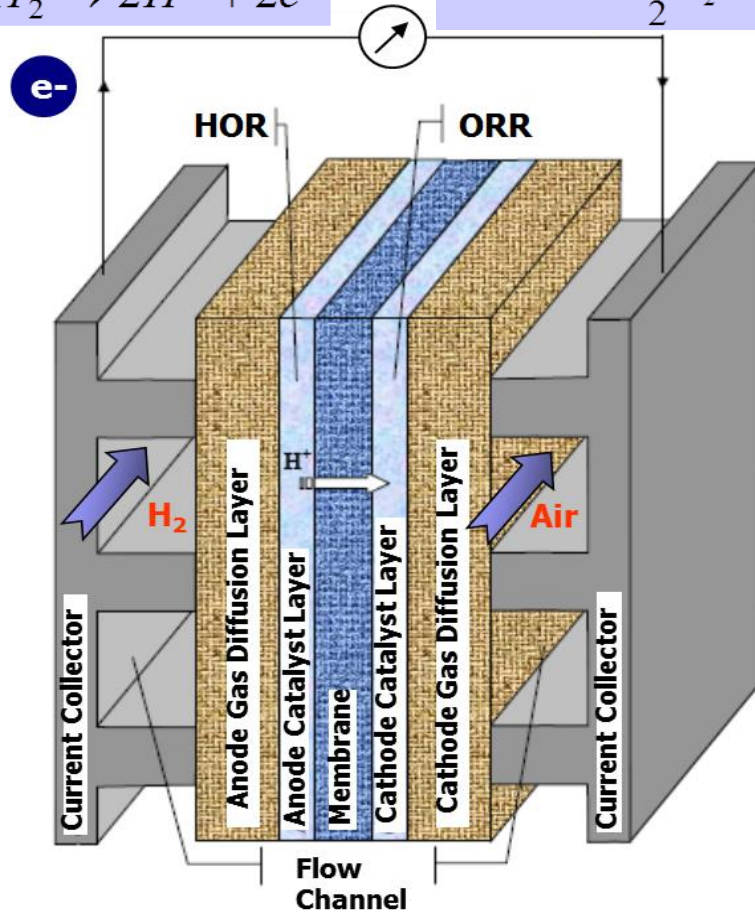
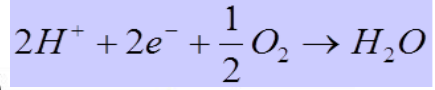
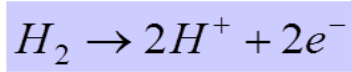


Figure 4. Operation and structure of a polymer electrolyte fuel cell (PEFC). (reprinted with permission from [31])

Although substantial theoretical and experimental research has been conducted in recent years for enhancing the overall PEFC performance, the catalyst layer remains least understood owing to its inherent complex structure and underlying multi-physical transport mechanisms. On the other hand, the three-decade long search for non-precious metal catalysts for the PEFC catalyst layer has so far revealed very few materials with promising activity in the rate-limiting ORR and performance stability.

Over the last decade, enormous research effort and resources have been devoted to overcoming several challenges in the development of PEM fuel cells for automotive propulsion. The main challenge toward realizing commercially viable hydrogen fuel cells hinges on the design and development of cheap and stable catalysts for the oxygen reduction reaction and low-cost manufacturing of innovative electrode architectures. Oxygen reduction catalysts used in current fuel cells are platinum nanoparticles supported on carbon black (Pt/C), but cost and supply constraints for large-scale adoption in automotive propulsion require a factor of >4 increase in catalytic activity per mass of precious metal.[32] In this context, the Pt-utilization target for 2015, as defined by the U.S. Department of Energy, is 0.2 g of Pt per kW at 55% efficiency for a transportation PEFC stack.[33, 34] Based on this target and under the assumption that all cars in the future would be powered by PEFCs, a global annual production of 100 million PEFC cars rated at 50 kW each would require a steady Pt demand of 1000 tons a year. In recent years, the global Pt production has only been *ca.* 200 tons a year, while the total world Pt reserves are estimated at 40,000 tons.[33, 34] Based on these

estimates, in order to maintain a sustainable PEFC based vehicle fleet, the Pt cost would likely rise significantly. One such forecast estimates that the Pt catalyst alone would account for 38–56% of the stack cost assuming a low Pt price of \$1,100 per troy ounce and a relatively low production volume of 500,000 PEFC stacks a year.[33, 34] Therefore, replacing platinum-based catalysts with a more abundant material would greatly improve the outlook for the widespread development of automotive fuel cells.

Non-precious metal catalysts using abundant transition metals have long been explored.[33] However, their viability relies on how close the electrochemical activity can be reached to that of traditional, but more expensive Pt/C catalysts. Most current work on non-precious metal oxygen reduction catalysts focus on nitrogen-coordinated iron in a carbon matrix. The nature of the active sites remains elusive. However, widely different synthesis methods produced virtually identical catalyst activities and PEM fuel cell performance continued to remain below that of Pt/C catalyst.[33] The most recent advancements in high-performance non-precious metal catalyst and electrode development have marked the dawn of a turning point.[35-38]

In order to accelerate the PEM fuel cell technology development and near-term market entry with particular focus on automotive applications, it is imperative to develop high performance electrodes with higher power density and lower cost. In this regard, a two-pronged research approach is warranted, which involves: (1) development of low-cost and less complicated manufacturing routes of novel electrode architectures using non-precious metal electrocatalysts with improved performance and durability; and (2)

gaining fundamental insight into complex structure-transport-performance interactions in the electrodes.

1.2.2 Precious metal catalyst: major cost driver of electrochemical cells

Precious metal (typically platinum) catalysts are essential in electrochemical cells for oxygen reduction reaction (ORR), but the expensive catalysts become one of the major hurdles in wide deployment of electrochemical cells. For instance, the catalyst cost of PEM fuel cells is nearly a half of the total cost (Figure 5), which is mainly because of the high price of platinum.[39] Therefore, there have been great efforts to develop non-precious metal catalysts over the past decades. Recently research outcomes suggest the platinum catalysts can be replaced by inexpensive nanomaterials such as complexes of nitrogen-doped carbon nanotubes or graphene with transition metals[40-45] although the exact mechanisms are yet to be revealed. Nevertheless, time-consuming multiple manufacturing steps for synthesizing these complexes become cost drivers, which will be addressed in this proposed research by employing the one-step synthesis process.

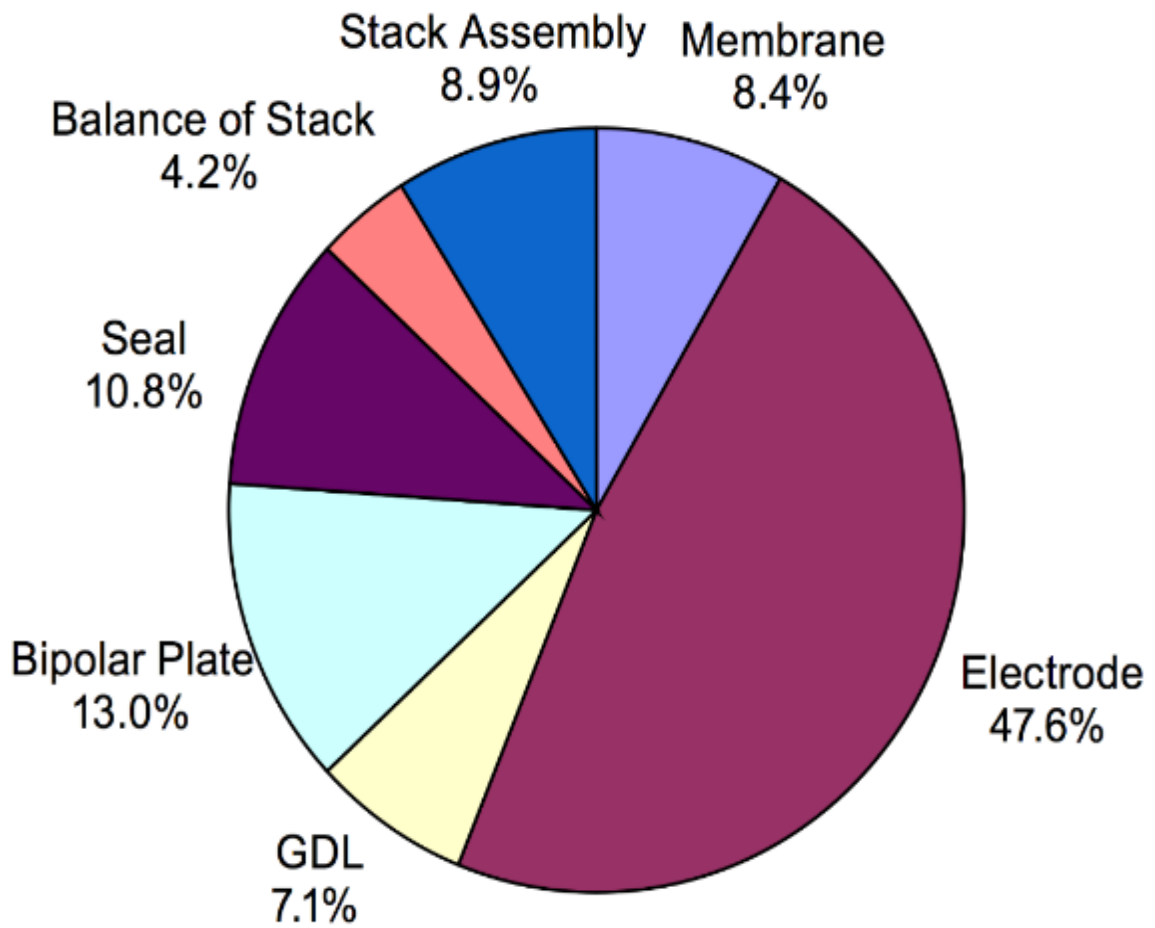


Figure 5. Manufacturing costs of major components in PEM fuel cells.[39] The high electrode cost is mainly due to the high price of platinum catalysts.

1.2.3 Transition metal catalysts for oxygen reduction

The reaction in the cathode is more than 100 times slower than that of the anode, where expensive Pt catalysts are necessary to overcome very slow reactions. Transition metals including Fe and Co are excellent candidates, due to their good reactivity and multiple valence states. The transition metals have good catalytic reactions, as schematically shown in figure 6. When oxygen is adsorbed on the transition metals, electrons are transferred from oxygen to the empty d_{z^2} orbitals of the transition metals, forming a δ bond (figure 6a). When electrons are transferred to cathodes during the fuel cell operation, electrons are donated to the anti-bonding π orbitals of oxygen (figure 6b), weakening oxygen-metal bonding and thereby increasing oxygen reactivity with proton (i.e., resulting in H_2O).[46]

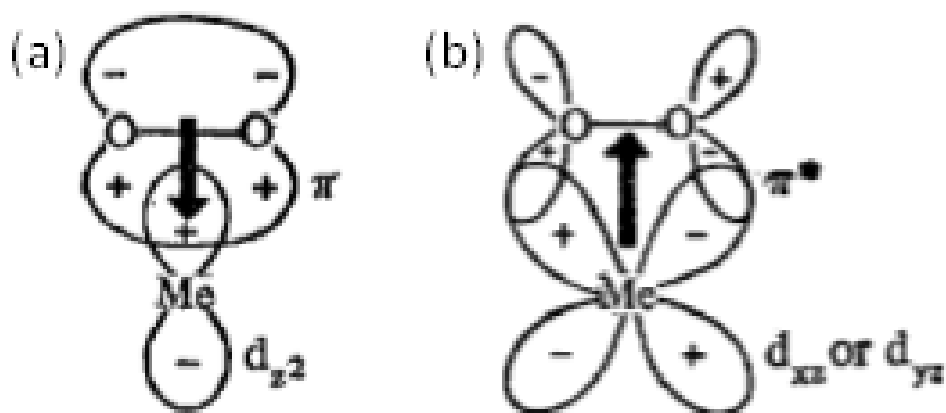


Figure 6. Schematic explanation of oxygen adsorption on a transition metal (a), and oxygen reduction by transferring electrons from the metal electrode to oxygen (b). (reprinted with permission from [47])

Despite the good oxygen reduction, the transition metals are easily oxidized in O_2 environment. The metal oxides are electrical insulators, prohibiting further charge transfer. Moreover, oxygen molecules hardly adsorb on the surface of the oxides.[48]

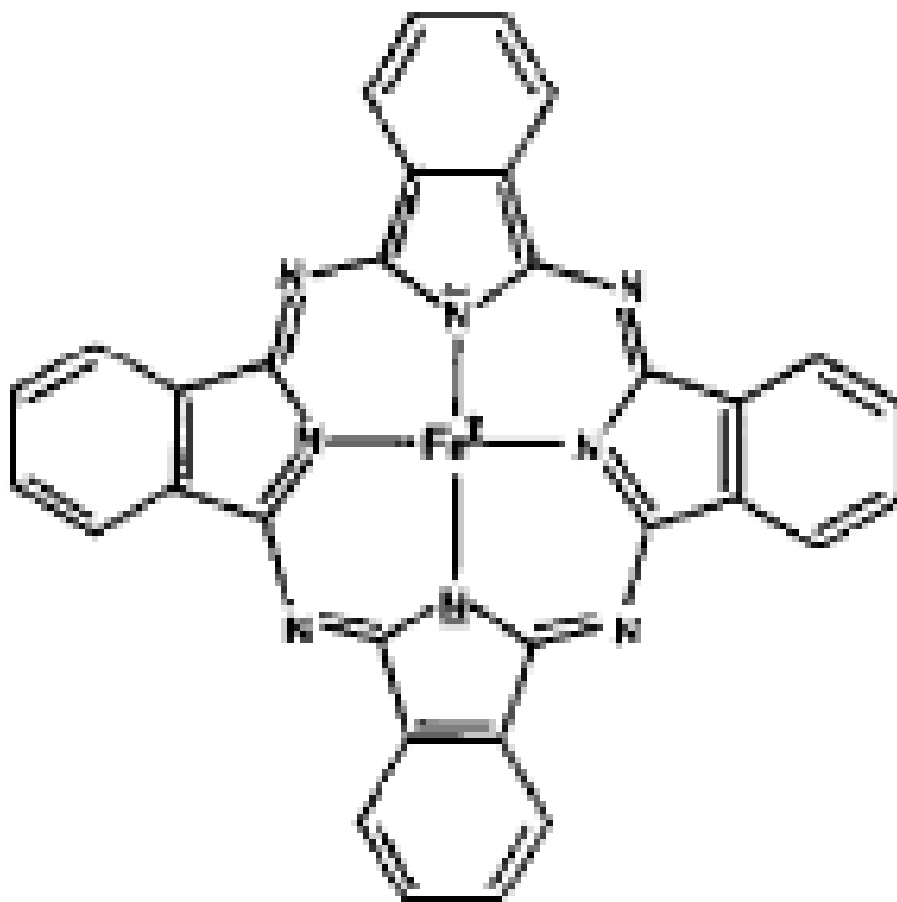


Figure 7. Fe(II)phthalocyanine, where Fe is surrounded by nitrogen and aromatic carbons.(reprinted with permission from [47])

The fast degradation of catalytic activities from the transition metals have been somewhat suppressed by surrounding the metal with organic molecules. Jasinski et al. reported for macrocyclic structure containing nitrogen-metal coordination as decent oxygen reduction reaction catalysts. Several non-noble transition metals such as Co, Fe, and Mn have been studied in the form of iron (III) phthalocyanine (figure 7) and cobalt tetramethoxy-phenylporphyrin (CoTMPP) for oxygen reduction reaction. Good oxygen reduction activities from the metal macrocycles are achieved,[49] but macrocycles still have poor stability. Therefore, additional heat treatment processes at high temperatures (above 1000 °C) were often performed to improve the durability by making stable protective graphitic layers.[50, 51]

1.2.4 Nitrogen-doped graphitic carbon structures for substituting precious metal catalysts

It has been demonstrated that nitrogen-doped graphitic structures have high catalytic activity for ORR.[40-45] The high electrical conductivity, exceptional mechanical property, and high surface area of the N-doped CNTs are ideal for exceptional ORR. For instance, the high surface area would create more active sites for ORR, leading to high current density in terms of per projected area. In order to improve the ORR catalytic activity of CNTs, nitrogen needs to be introduced into the structure, which is believed to promote the oxygen adsorption kinetics as well as the electron transfer from the electrode to the oxygen.[43-45] Moreover, it has been reported that

with the transition metal incorporation, the catalytic performance of N-doped graphitic carbon would significantly improve.[37, 38, 52] It has been reported that the ratio of pyridinic nitrogen to graphitic nitrogen is the most important parameter in improving the performance of nitrogen-doped, carbon-based catalysts for ORR.[43, 45] Nevertheless, the exact mechanism underlying the performance improvement has not been fully understood, the catalytic activity improvement has been clearly demonstrated by different groups including the PI. The catalytic activities with the N-doped with Fe nanoparticles will be studied both theoretically and experimentally through the proposed research, which will reveal the catalytic activities behind improved ORR performance.

1.3 Carbon nanotubes polymer composite by microwave heating

1.3.1 Carbon nanotubes polymer composite aerogel

Carbon materials have used to make aerogel because of their high strength and electrical conductivity[53-56]. In particular, carbon nanotubes(CNTs)-based aerogel materials have high electrical properties and large surface area, and is promising candidate for super-capacitors and battery electrodes[57, 58]. However, the drawback is fragility and relatively poor mechanical properties under compressive environment, which largely limits the utilization of carbon-based aerogel[30, 59], similar as other inorganic aerogels. Thus, strengthening process should be required to improve their mechanical properties.

Generally, hybridization with polymers is a typical method for the improvement of mechanical properties of aerogel[30, 60, 61]. Poly(vinyl alcohol) (PVA)[30], epoxy[30], and cellulose[62] are commonly used as polymer. Carbon-based polymer composite aerogel clearly show the improvement in mechanical properties, but flexibility and elasticity are demand properties in many applications, such as inflatable decelerators[63]. To make the elastic aerogels, other research groups have developed CNTs-PDMS composite aerogel using infiltration method[53, 64], but the infiltration method led to decrease pore size in aerogel because polymer fills the aerogel pores. In this study, the facile and quick process has been designed to fabricate the CNTs-polymer composite aerogel with minimizing pore loss by microwave irradiation.

In particular, carbon materials are excellent absorbers of microwave radiation, so they are easily heated by microwave [65-67], and several studies have reported that strong heat release from CNTs under microwave irradiation easily makes a high temperature within a period of seconds [68-70]. In the matter of as-synthesized CNTs, it usually has structural imperfections, which cause the decline of ballistic transport, allowing the Joule heating in CNTs. A simple model to describe microwave-induced heating of CNTs has been suggested by conversion of electromagnetic energy into mechanical vibration [71]. According to this model, CNTs exposed to microwave radiation have ultra-heating because of a transverse parametric resonance, resulting in the polarization of CNTs in the microwave field. Inspired by this approach, our hypothesis is that the PDMS-CNTs nanocomposite aerogel is possibly fabricated by microwave irradiation with minimizing pore loss.

1.3.2 The advantages of microwave heating

Microwave is the electromagnetic radiation with frequencies in the range of 300 MHz to 300 GHz. The microwave is extensively used in a wide range of applications, such as industrial, medical, and scientific equipment [65, 72]. In terms of materials processing, microwave irradiation is a well-known heating processing that the interaction of charged particles in materials with electromagnetic radiation causes the materials to heat up, and allows energy dissipation by the emission of heat [65, 72, 73]. Microwave heating has several advantages compared with the conventional heating such

as non-contact heating, rapid heating process, and selective material heating, as shown in figure 8. Because of these advantages, microwave heating process is extensively used in many industrial and scientific fields. In particular, carbon materials are excellent absorbents of microwave radiation, so they are easily generated heat by microwave[65-67], and several studies have reported that strong heat release from CNTs under microwave irradiation easily make a high temperature within a period of seconds[68-70]. In the matter of as-synthesized CNTs, it usually has structural imperfections, which cause the decline of ballistic transport, allowing the Joule heating in CNTs. A simple model to describe microwave-induced heating of CNTs has been suggested by conversion of electromagnetic energy into mechanical vibration[71]. According to this model, CNTs exposed to microwave radiation have ultra-heating because of a transverse parametric resonance, resulting in the polarization of CNTs in the microwave field[67].

Microwave heating is produced by converting the electromagnetic energy to thermal energy. It has several advantages typical heating processes, such as rapid heating, reduced process time, low-cost, and selective heating in the material[74]. Especially, microwaves can transport their energy directly to materials by radiation without conduction and convection which are main processes of energy deliver in normal heating methods. Therefore, microwave heating is faster than typical heating processes, and selective heating is possible. The application of microwave heating is general heating processes such as drying[75], sintering[76], and curing of rubber[77]. In

general, energy consumption of microwave heating is less than other heating processes and the process time is also shorter.

Materials which react with microwaves to make heat are called microwave absorbing materials[65]. Most of all, carbon nanotubes are strong microwave absorbing material which can produce intense heating[78]. Carbon nanotubes have outstanding electrical properties since sp^2 bonding[25, 55, 79]. So, the number of free electrons can move over the whole layer is approximately one per each carbon atom[80]. Free electrons enable carbon nanotubes to absorb microwave. Thus, carbon nanotubes can be used as microwave absorber which can supply heat to other materials by conduction and radiation. In addition, it is possible to enhance a heating efficiency by the decoration of nano-sizes metal particle on carbon nanotubes since nano-sizes metal powder react properly with microwave[81]. To deposit metal nanoparticles, electroplating, galvanic displacement method[82, 83], and physical methods are commonly used[84].


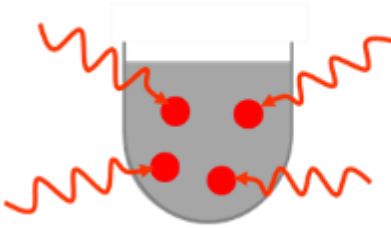
Heating method	Heat introduction
Conventional heating	
Microwave heating	

Figure 8. Schematic of heat introduction for conventional heating and microwave heating

Microwave heating process enable the heating process times to be over 5 times faster compared to conventional heating[85, 86] due to extremely high heating rate[87]. Microwave heating is basically different from conventional heating. The surface of materials is initially heated the surface of materials in conventional heating by the convection and radiation, after that, the transfer of thermal energy to the inside of

materials is occurred by conduction. On the other hand, in the case of microwave heating, the microwave energy is directly converted to thermal energy through the volume of the material, known as volumetric heating, which is highly energy efficient since microwave is only heated the material, not the air around it. General microwave energy efficiency is approximately 50%, which is higher than that of conventional fuel-fired heating, which is generally 10 to 30% [85, 86]. Therefore, microwave heating can be reduced production costs and energy consumptions.

CHAPTER II

ONE-STEP SYNTHESIS OF NITROGEN-IRON COORDINATED CARBON NANOTUBE CATALYSTS FOR OXYGEN REDUCTION REACTION*

2.1 Introduction

Oxygen reduction reaction (ORR) is a key reaction occurred in many electrochemical cells such as fuel cells and metal-oxygen batteries.[38, 88-92] Sluggish ORR typically necessitates precious metal based catalysts whose high prices have been major challenges for commercial applications.[38, 93-95] Over the past several years, various non-precious metal based nanomaterials have been suggested to reduce the cost of the catalysts, but these catalysts involve complicated synthesis processes, significantly increasing the manufacturing cost.[96, 97]

Among the recently developed catalysts, nanostructured carbon with transition metals and nitrogen has been notable due to their high catalytic activity, low cost, and good durability.[88, 96, 98-101] Nevertheless, high manufacturing costs due to complicated synthesis processes negate the benefit of eliminating the precious metal catalysts, as summarized in Table 1. For instance, remarkable ORR activity was

* Reprinted with permission from W. Choi, G. Yang, S. L. Kim, P. Liu, H.-J. Sue, C. Yu, One-step synthesis of nitrogen-iron coordinated carbon nanotube catalysts for oxygen reduction reaction, *J. Power Sources*, 313, 128-133, Copyright 2016 by Elsevier. [104]

observed from nitrogen/iron-doped carbon catalysts with graphene structure[101] and polyaniline-derived carbon catalysts,[38] but time-consuming polymerization processes and additional leaching steps were necessary to remove inactive materials. Fewer steps with less synthesis times were reported for nitrogen-doped graphene[102] and Co_3O_4 -coated on graphene,[103] but they still required lengthy and complicated manufacturing processes compared to those of Pt/C based catalysts.

Herein, we report a simple one-step process to synthesize iron/nitrogen-coordinated CNT catalysts. Our precious metal free catalysts showed high ORR activity and long-term stability comparable to those of Pt based commercial catalysts. Furthermore, a series of experimental analyses have unveiled the reason behind the high ORR performance of our catalysts, which is often missing in literature but important to further improve and modify the catalysts.

2.2 Experimental section

2.2.1 Synthesis and characterization

A precursor solution to synthesize CNT catalysts (labeled as Fe-A/P-CNT in Table 1) were made by dissolving ferrocene powders (Sigma-Aldrich, 98%) in a 1:1-ratio mixture of aniline (Alfar Aesar, 99+%) and pyridine (Alfa Aesar, 99+%) with a concentration of 60 mg ferrocene per mL. Aniline and pyridine were used to obtain a nitrogen-doped graphitic structure, and iron from ferrocene was used as a catalyst to grow CNTs as well as N-Fe-C coordination for a high catalytic activity.[92] To compare the influence of nitrogen doping precursors, we also used aniline only (labeled as Fe-A-CNT in Table 2) or pyridine only (labeled as Fe-P-CNT in Table 2) instead of mixing half and half. Additionally, to investigate the influence of iron coordination, CNTs were grown without incorporating iron during the growth of CNTs (labeled as A/P-CNT in Table 1), and nitrogen doping effects were studied by growing CNTs using nitrogen-free C_2H_4 instead of aniline or pyridine (labeled as Fe-CNT in Table 2).

To synthesize the samples except Fe-CNT, a quartz tube whose inner diameter is 22 mm was initially purged with 900-sccm Ar (Airgas, 99.999%). The quartz tube was placed in a three-zone tube furnace (Lindberg Blue M, Thermo Scientific) whose target temperatures for the 1st and 3rd zones were set to 250 °C and 950 °C, respectively. The tip of a needle for feeding the precursor solution was located at the middle of the 1st zone. After the target temperatures were reached in ~12 min, 250-sccm H_2 (Airgas,

99.999%) was added to the Ar flow. The mixture solution was continuously injected into the furnace tube with a rate of 0.1 mL min^{-1} using a syringe pump. After finishing the reaction, the Ar flow rate was decreased to 100 sccm while the hydrogen flow was turned off. The products were gathered after the quartz tube was cooled to room temperature. Typically, ~ 100 -mg catalysts were obtained with 20-min reaction time. To have A/P-CNT, iron (6 nm) and aluminum (10 nm) films were deposited as catalyst layers to grow CNTs[90] using an e-beam evaporator on a Si wafer. A mixture of aniline and pyridine (1:1 by volume) without ferrocene was used as a precursor solution. Except ferrocene in the precursor solution, other synthesis conditions to obtain A/P-CNT were the same as those for other Fe/N-containing CNT catalysts.

To synthesize Fe-CNT, an alumina crucible filled with 120-mg ferrocene was placed in the 1st zone, and 120 and 800 °C were set for the 1st and 3rd zone of the tube furnace with a ramping rate of 80 °C min^{-1} . Initially 200-sccm Ar was flowed until the target temperatures were reached, and then 80-sccm C₂H₄ (Airgas, 99.999%) and 200-sccm H₂ were added to the Ar flow. After 20 min reaction, ~ 30 mg of Fe-CNT catalysts was typically obtained.

The morphology of the samples was inspected using a scanning electron microscope (SEM, FEI Quanta 600) and transmission electron microscope (TEM, JEOL JEM 2010). The composition of the samples was analyzed using X-ray photoelectron spectroscopy (XPS, Omicron ESCA+) with a charge correction by carbon 1s at 284.8 eV as a reference as well as thermogravimetric analysis (TGA, TA Instruments Q500) at

40~900 °C in air with a heating rate of 5 °C min⁻¹. Raman spectroscopy analysis was conducted by Horiba Jobin-Yvon LabRam Raman Confocal Microscope to study the graphitic nature of CNTs.

Table 2. List of catalysts and corresponding precursors used for synthesis. The samples were grown on quartz plates except A/P-CNT, which was grown from Fe (6 nm)/Al (10 nm) deposited Si wafers.

Sample name	Precursors
Fe-A/P-CNT	Ferrocene, Aniline, Pyridine
Fe-A-CNT	Ferrocene, Aniline
Fe-P-CNT	Ferrocene, Pyridine
A/P-CNT	Aniline, Pyridine
Fe-CNT	Ferrocene, C ₂ H ₄

2.2.2 Electrochemical measurements

The catalyst samples (7 mg) were dispersed in a mixture of DI water (500 μL), ethanol (170 μL, 92-94%, EMD Millipore), and 5-wt% Nafion solution (160 μL, Fuel cell earth) with a pen type sonicator (FB-120, Fisher Scientific) with 120 W for 10 min. The catalyst ink (5 μL) was loaded on a glassy carbon electrode (BASi) whose active electrode area was 7.07 mm² (3 mm in diameter), and then dried in an oven at 40 °C for

120 min. For comparison, commercial Pt/C (20-wt% Pt, Fuel cell earth) was also made into ink with the same method.

Rotating disk electrode (RDE) and cyclic voltammetry (CV) experiments (604D CHI electrochemical station) were performed in 0.1 M KOH electrolyte with an Ag/AgCl electrode in saturated KCl (0.197 V *vs.* SHE) as a reference electrode, a Pt wire as a counter electrode, and the samples as a working electrode. Oxygen or nitrogen (100 sccm) was continuously purged to the electrolyte, and CV and RDE tests began after 30 min gas purging. In the RDE test, the working electrode was rotated with variable rotating speeds of 850 ~ 1600 rpm at -1.0 ~ 0.2 V *vs.* Ag/AgCl with a scan rate of 5 mV s⁻¹. In the CV test, the measurement was conducted at -1.2 ~ 0.2 V *vs.* Ag/AgCl with a scan rate of 100 mV s⁻¹.

2.3 Results and Discussion

2.3.1 Morphology and material structure

As-synthesized Fe-A/P-CNT consists of aligned wavy CNTs whose lengths are over 100 μm (Figure 9a). The CNTs have iron-containing nanoparticles and graphitic layered structures whose outer diameters are 30~70 nm (figure 9b and c). The curved graphitic layers may come from nitrogen doping in graphitic carbon, which may create curvatures in the graphene sheets due to pentagonal defects.[105] With a single nitrogen-containing precursor, Fe-A-CNT samples also had wavy CNTs with larger curvatures (figure 9d), but those in Fe-P-CNT were rather straight (figure 9e). When iron was not delivered during the growth of CNTs for A/P-CNT, the CNT packing density was found to be higher than those of other iron/nitrogen-containing samples (figure 9). The morphology of Fe-CNT samples is similar to that of Fe-A-P-CNT (figure 9g), but iron and nitrogen were not incorporated during the CNT synthesis process.

According to the intensity ratio (I_D/I_G) of D-band ($\sim 1330\text{ cm}^{-1}$) to G-band ($\sim 1580\text{ cm}^{-1}$) in the Raman spectra (Figure 10), the nitrogen-containing aniline and pyridine precursors resulted in higher intensity ratios compared to that of Fe-CNT, suggesting higher defect densities in the graphitic carbon structure.[92, 106] I_D/I_G from Fe-A-CNT was the highest (1.41), and I_D/I_G from Fe-A/P-CNT was 1.39, which is in the middle of those from Fe-P-CNT (1.21) and Fe-A-CNT. It was noticed that the waviness of CNTs shown in SEM images (see figure 9) was intensified as I_D/I_G gets higher. The CNTs in

Fe-A-CNT have large curls in comparison to relatively straight CNTs in Fe-A/P-CNT, and the CNTs in Fe-A/P-CNT have those in between. These intensity ratio values were much higher than 0.82 from Fe-CNT, indicating nitrogen doping in the graphitic carbon structure.[92, 106-108]

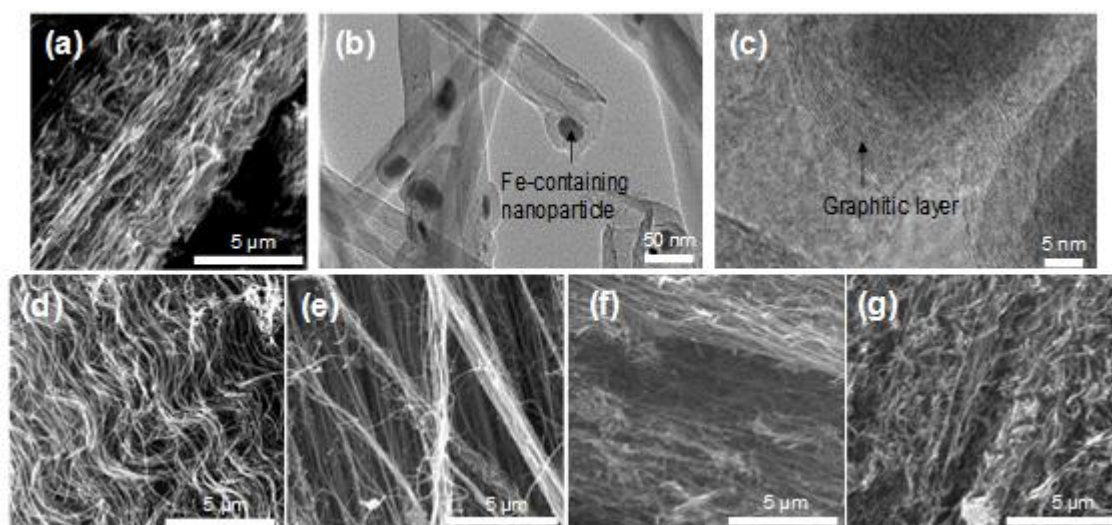


Figure 9. The SEM and TEM images of Fe-A/P-CNT (a)~(c), Fe-A-CNT (d), Fe-P-CNT (e), P-A-CNT (f), and Fe-CNT (g).

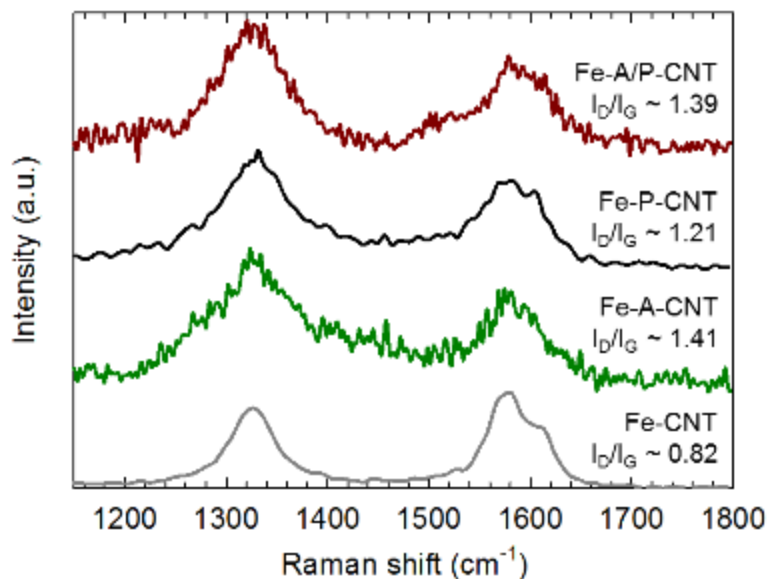


Figure 10. Raman spectra of the iron-incorporated CNTs and the intensity ratio of D-band to G-band (I_D/I_G).

2.3.2 Electrochemical analysis

The RDE test results in figure 11a show Fe-A/P-CNT has lower onset potential than that of Pt/C with a slightly lower half-wave potential (~ 72 mV difference), which is similar to the performance of other non-Pt based catalysts.[102, 103, 109-111] Nevertheless, the current density of Fe-A/P-CNT at a cell voltage of 0.3 V where alkaline fuel cells (e.g., direct methanol fuel cells) typically operate[112] is -6.7 mA/cm², which is slightly higher than that of Pt/C (-5.8 mA/cm²). Significantly lower onset potentials were observed from A/P-CNT and Fe-CNT, suggesting both nitrogen

and iron are necessary to have high catalytic activity. In addition, A/P-CNT appears to have the two-step oxygen reduction reaction with onset potential at -0.36 V and -0.64 V.[113] The larger limiting current density from Fe-A/P-CNT compared to that of Pt/C suggests the large specific area of electrochemically active sites on the Fe-A/P-CNT.[114, 115] It is interesting to see nitrogen doping by both aniline and pyridine resulted in better performances than those with a single dopant, aniline or pyridine.

The high catalytic activity of Fe-A/P-CNT was also confirmed from CV results (figure 11b). Fe-A/P-CNT has the ORR peak at -0.32 V in the oxygen environment, and this ORR reaction was confirmed by no ORR peaks in the nitrogen-saturated CV result. The maximum current density and peak potential for Fe-A/P-CNT were also larger than those of the samples with only one precursor (aniline or pyridine). The maximum current for Fe-A/P-CNT was even larger than that of Pt/C, and relatively poor performances from nitrogen- or iron-deficient samples (no iron for A/P-CNT and no nitrogen for Fe-CNT) were observed (figure 11c).

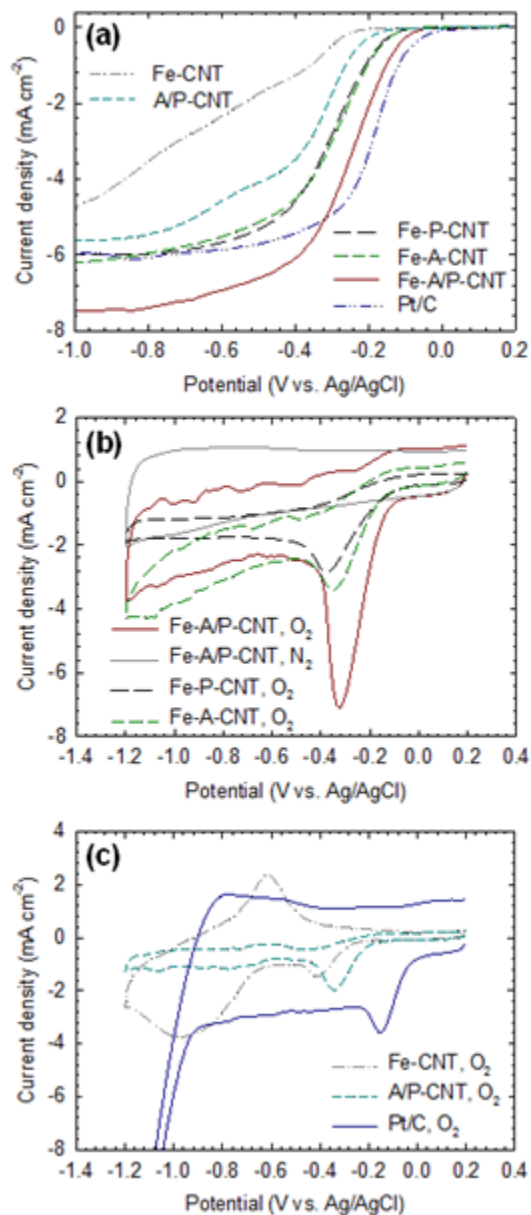


Figure 11. (a) RDE polarization curves of Fe-CNT, A/P-CNT, Fe-P-CNT, Fe-A-CNT, Fe-A/P-CNT, and Pt/C in O₂-saturated 0.1 M KOH electrolyte with 1600 rpm and 5 mV s⁻¹, respectively. (b) CV results of Fe-A/P-CNT, Fe-P-CNT, and Fe-A-CNT in N₂- and O₂-saturated 0.1 M KOH electrolyte with a scan rate of 100 mV s⁻¹. (c) CV results of Fe-CNT, A/P-CNT and Pt/C in O₂-saturated 0.1 M KOH electrolyte with a scan rate of 100 mV s⁻¹.

The nitrogen and iron doping essential to high ORR activity was further analyzed by XPS. According to the XPS survey scan and analysis (figure 12 and Table S1), the nitrogen at%’s for Fe-A/P-CNT, Fe-A-CNT, and Fe-P-CNT are similar, but the iron at% of Fe-A/P-CNT is 8.6 times higher than that of Fe-A-CNT and 3.8 times higher than that of Fe-P-CNT (table 3). The relative ratios of iron in the samples are quite different from the TGA result (table 3 and figure 13). For example, according to TGA results, the iron wt% of Fe-A/P-CNT is only 1.5 times higher than that of Fe-A-CNT (Table S1). We believe this different result is caused by different analysis methods of XPS and TGA. For example, XPS is designed to probe sample surfaces, and therefore it is ideal to analyze nitrogen-coordinated iron that is often present on the wall (graphitic layer) of CNTs. On the other hand, iron-containing particles embedded deep inside the CNTs can be detected by TGA rather than XPS.

Table 3. TGA and XPS analysis of Fe-P-CNT, Fe-A-CNT, and Fe-A/P-CNT.

Sample	TGA		XPS	
	wt% of Fe	at % of Fe	at% of N	
Fe-P-CNT	4.4	0.25	1.53	
Fe-A-CNT	4.2	0.11	1.74	
Fe-A/P-CNT	6.4	0.95	1.34	

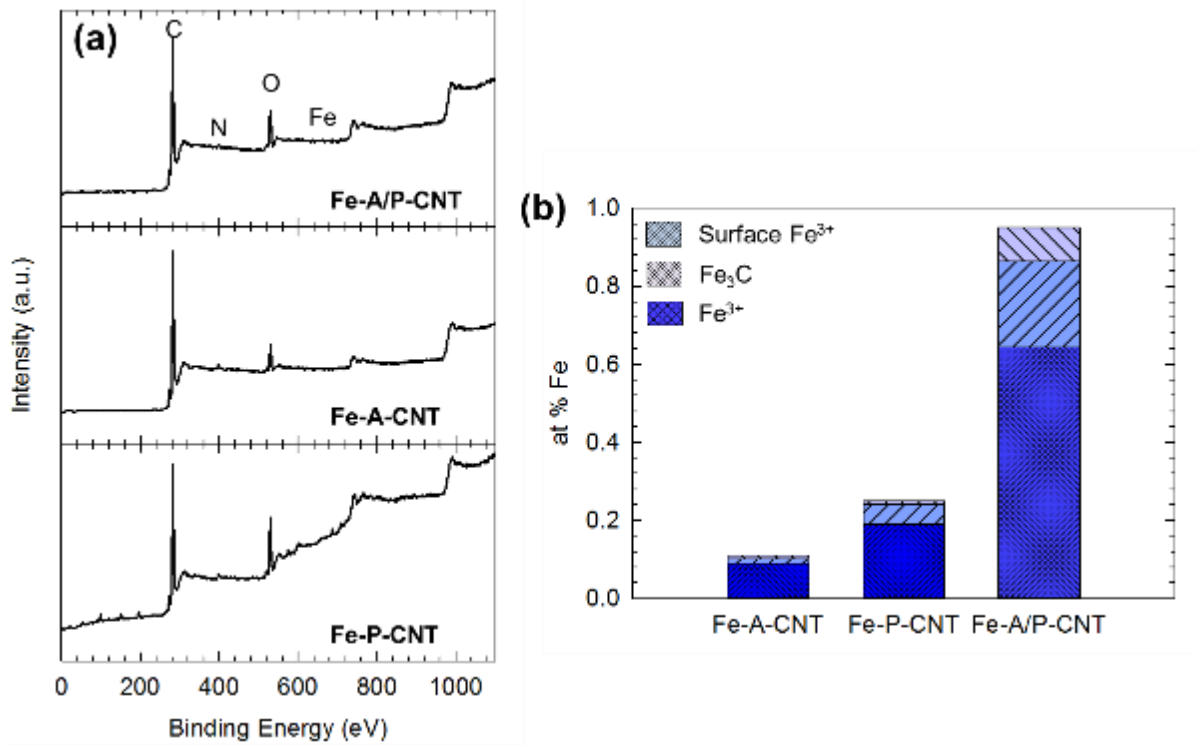


Figure 12. (a) Survey XPS scan results of Fe-A/P-CNT, Fe-A-CNT, and Fe-P-CNT. (b) The comparison of iron atomic concentration of doped carbon nanotubes.

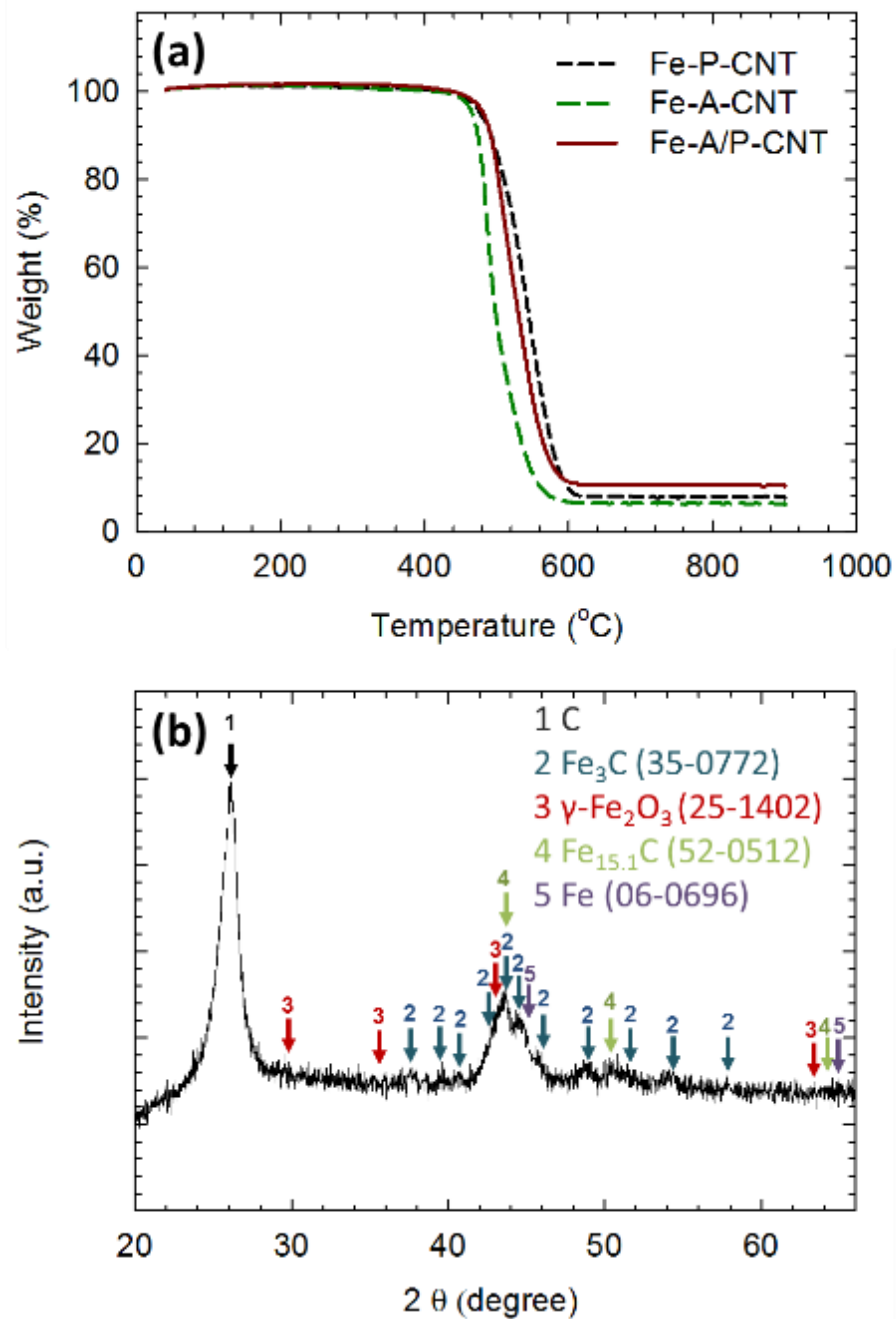


Figure 13. (a) TGA results of Fe-P-CNT, Fe-A-CNT, and Fe-A/P-CNT. (b) XRD result of Fe-A/P-CNT.

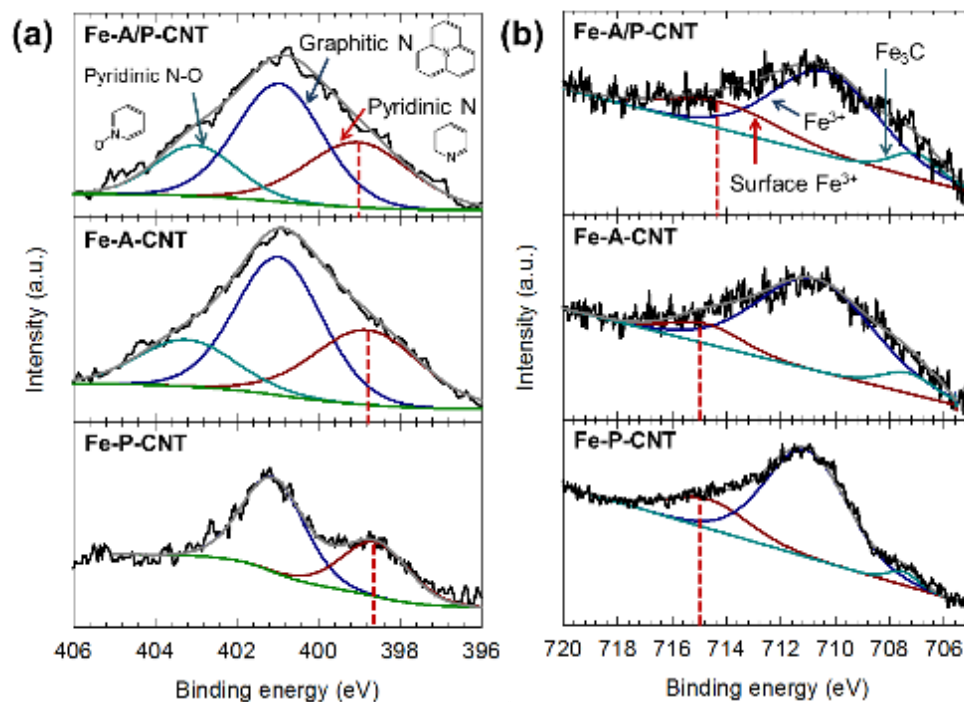


Figure 14. (a) N-1s XPS results of Fe-A/P-CNT, Fe-A-CNT and Fe-P-CNT. The vertical broken lines indicate the peak location of pyridinic nitrogen. (b) Fe-2p XPS results of Fe-A/P-CNT, Fe-A-CNT and Fe-P-CNT. The vertical broken lines indicate peak location of surface Fe³⁺.

Figure 14a shows N-1s XPS spectrum, which can be separated into pyridinic N at ~398.8 eV, graphitic N at ~400.9 eV, and oxidized pyridinic N at ~403.2 eV.[116-119] A notable difference in the N-1s spectra is the shift of the peak corresponding to the pyridinic nitrogen of Fe-A/P-CNT to a higher binding energy, compared to those of Fe-A-CNT and Fe-P-CNT, indicating nitrogen coordination with iron.[92, 120, 121] The Fe-2p spectrum can be also separated into Fe₃C at ~707.1 eV, bulk Fe³⁺ at ~710.6 eV,

and surface Fe³⁺ at ~714.2 eV (figure 14b).[91, 122, 123] The peak shift of the surface Fe³⁺ in Fe-A/P-CNT toward a lower binding energy also indicate the stronger coordination of iron with pyridinic nitrogen.[92, 122, 123]

RDE tests of Fe-A/P-CNT at different rotational speeds were performed (figure 15a), indicating the four-electron reaction according to the Koutckey-Levich plot at various potentials (figure 15b). The Koutecky-Levich plots[91, 124] were obtained by using $J^{-1} = J_K^{-1} + B^{-1}\omega^{-1/2}$ and $B = 0.62 nFC D^{2/3}\nu^{-1/6}$, where J_K^{-1} is kinetic limiting current density, ω is the rotational speed, n is the number of electrons transferred, F is the Faraday constant ($F = 96,500 \text{ C mol}^{-1}$), C is the bulk concentration of O₂ ($C = 1.2 \times 10^{-6} \text{ mol cm}^{-3}$ in 0.1 M KOH), D is the diffusion coefficient of O₂ ($D = 1.9 \times 10^{-5} \text{ cm}^2 \text{ s}^{-1}$ in 0.1 M KOH), and ν is the kinematic viscosity of the electrolyte ($\nu = 0.01 \text{ cm}^2 \text{ s}^{-1}$ in 0.1 M KOH).[92, 125, 126] The number of electrons transferred (n) is 3.97.

The good long-term stability of Fe-A/P-CNT was confirmed in the RDE test. 30,000 cycles in oxygen-saturated 0.1 M KOH. After 30,000 cycles, the decrease of the half-wave potential for Fe-A/P-CNT and Pt/C were 64 mV and 71 mV (figure 15c), respectively, and the limiting current density of Fe-A/P-CNT dropped ~10 %, which is similar to or better than the recent reports.[88, 127] In addition, the half-wave potential for Fe-A/P-CNT is higher than nitrogen doped carbon based nanostructures[119] and nitrogen doped graphene.[128] These results demonstrate the good stability of Fe-A/P-CNT for oxygen reduction reaction.

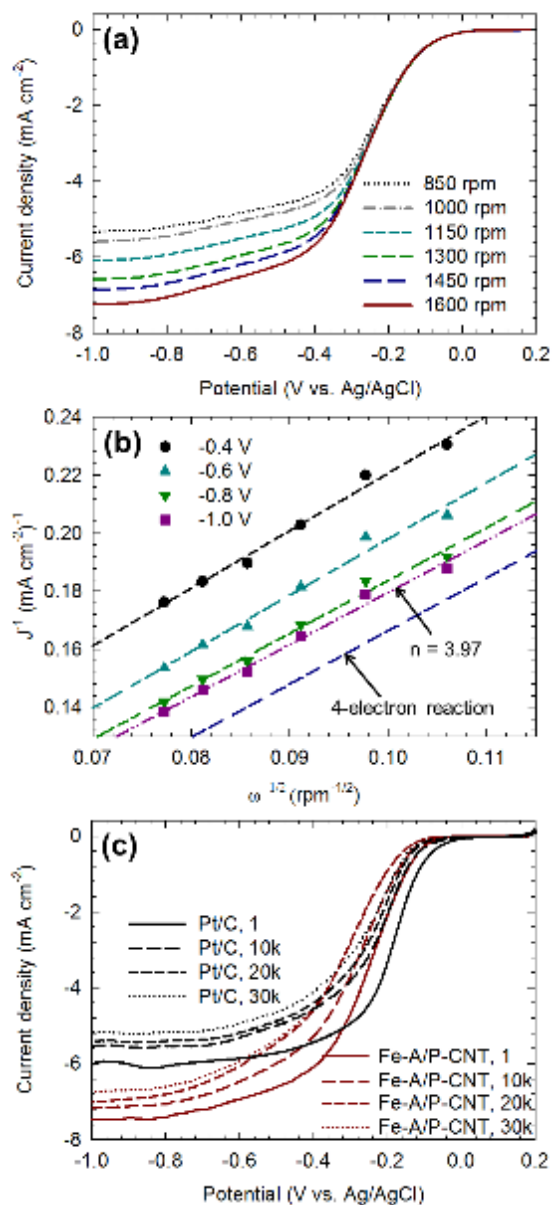


Figure 15. (a) RDE polarization curves of Fe-A/P-CNT in O₂-saturated 0.1 M KOH electrolyte at 6 different rotational speeds of the electrode, starting from 1600 rpm to 850 rpm (every 150 rpm). (b) The Koutecky-Levich plots for Fe-A/P-CNT from the RDE results. (c) The RDE polarization curves of Fe-A/P-CNT were compared with those of commercial Pt/C before and after 10000, 20000, and 30000 CV cycles. The rotating speed and the scan rate were 1600 rpm and 5 mV s⁻¹, respectively.

2.4 Conclusions

We synthesized nitrogen and iron doped CNTs for oxygen reduction reaction by one-step synthesis. Fe-A/P-CNT showed significantly high electrocatalytic activity and long-term stability comparable to those of Pt based commercial catalysts. We identified that the coordination of nitrogen and iron in carbon based nanostructures played a key role in achieving the high ORR performances by comparing catalytic activities of different CNT catalysts synthesized with/without iron and/or nitrogen from aniline and pyridine. We anticipate further study in our one-step synthesis process may result in scalable mass production of non-precious metal catalysts for a broad range of electrochemical cells.

CHAPTER III
ULTRA-RESILIENT CARBON NANOTUBE COMPOSITES AEROGEL WITH
THERMAL INSULATION AND ELECTRICAL PROPERTIES BY MICROWAVE
IRRADIATION

3.1 Introduction

An aerogel is highly porous material with low density, low thermal conductivity, a three-dimensional structure, and large surface area and has potential applications, such as thermally insulation materials, mechanical actuators, and medicine[30, 129]. In particular, the outstanding characteristic of aerogel is a low thermal conductivity, for example, traditional silica aerogel shows $\sim 30 \text{ mW m}^{-1}\text{K}^{-1}$ [130]. Recently, many kinds of aerogel have been developed, but most of them are made from silica, metal oxide, and polymer[53, 131]. Furthermore, many applications require much more functionalities, such as electrical properties, compressibility, and robustness under mechanical stress[53]. With the development of nanotechnology, silica-based aerogels are fabricated, but they are insulator, fragile, and difficult to make in large size[62].

Nowadays, carbon materials have used to make aerogel due to their high strength and electrical conductivity[53-56]. Most of all, carbon nanotube(CNT)-based aerogel materials have high electrical properties and large surface area, and is promising candidate for super-capacitors and battery electrodes[57, 58]. Graphene and graphene

composite aerogels are also useful in various advanced application, such as sensors. However, like other inorganic aerogels, the main disadvantage is fragility and relatively poor mechanical properties under stress loading environment, which largely restrict the utilization of carbon-based aerogel in many applications [30, 59]. Thus, strengthening methods should be required to improve their mechanical properties.

In general, hybridization with polymers is a typical method for the mechanical improvement of aerogel[30, 60]. Poly(vinylalcohol) (PVA)[30], epoxy[30], and cellulose[62] are frequently used as polymer. Carbon-based aerogels with polymers clearly show the improvement in mechanical strength, but flexibility and elasticity are demand properties in many applications, such as inflatable decelerators[63]. To fabricate the elastic aerogels, other research groups have fabricated CNT-PDMS composite aerogel using infiltration method[53, 64], but the infiltration method led to decrease pore size in aerogel since polymer fills the aerogel pores. Instead of infiltration method, microwave irradiation was used to fabricate CNT-PDMS composite[73]. Carbon materials are excellent absorbents of microwave radiation, so they are easily generated heat by microwave[65-67], and this heat leads to the localized thermal welding of CNT to polymer within a few second[73]. Inspired by this approach, our hypothesis is that the PDMS-CNT composite aerogel is possibly fabricated by microwave irradiation with minimizing pore loss.

In this work, we designed the facile and quick process for the scalable production of super resilient CNT-PDMS composite aerogel with ultra-low thermal conductivity and

high electrical properties by microwave heating. This report describes that the microwave heating process can lead to a quick reaction and allow for the uniform polymer layer on CNT, which enhance the mechanical properties of carbon nanotube composite. Furthermore, the nanometer-thickness PDMS layer coated CNT sponge shows high compressibility, thermal insulation and elasticity-dependent electric conduction, suggesting its use as promising high mechanical properties with shows ultra-low thermal conductivity and high electrical conductivity in a wide range of real-world applications.

3.2 Experimental section

3.2.1 Carbon nanotube sponge synthesis

Carbon nanotube(CNT) sponge were synthesized by a chemical vapor deposition (CVD) method reported by us previously.[79] An alumina crucible boat containing ~ 0.3 g ferrocene (Sigma-Aldrich, 98%) was located in zone 1 (upstream) of a quartz tube with an inner diameter of 22 mm. Before the growth, argon (Airgas, 99.999%) gas was flowed for 10 min as a purge gas. During the growth reaction, hydrogen (Airgas, 99.999%), ethylene (Airgas, 99.999%), and argon gases were flowed into the tube at flow rates of 260 sccm, 80 sccm, and 80 sccm, respectively. The argon gas was passed through a bubbler filled with deionized (DI) water. The temperatures of zone 1, zone 2, and zone 3 (CNT growth zone) were 120 °C, 120 °C, and 650 °C, respectively. The typical growth time was 30 min to get approximately 80~90 mm long sponge shown in Fig. 1a. After the growth reaction, the furnace (Lindberg Blue M, Thermo Scientific) was naturally cooled under 100 sccm argon flow to room temperature.

3.2.2 Carbon nanotube - PDMS composite fabrication

The schematic fabrication process is described in Fig. 1a. In a typical process for the fabrication of CNT- Polydimethylsiloxane (PDMS) composite aerogel, CNT sponge was cut into 12.7 mm in diameter and 2~3 mm in length and then soaked in PDMS (Sylgard 184, Dow Corning) - hexane (60% n-Hexane, VWR) mixture solution by

magnetic stirring for 3 hours at 300 rpm using magnetic stirrer (Isotemp Hotplate Stirrer, Fisher Scientific). To compare the influence of PDMS content, we used different weight ratio of PDMS - hexane mixture solution. After the immersion of CNT sponge in PDMS-hexane solution, the microwave heating process was conducted in a microwave oven (EM925AJW-P1, WestBend) with an output power of 900 W. The process was carried out 5 times with 3 second using 50% power of microwave to make thin PDMS layer on CNT surface. After the microwave heating, composite was sonicated for 1 min in hexane for removing unsolidified PDMS residue and then composite was dried in convection oven (Series FP, Binder Inc.) for 30 min at 150 °C.

3.2.3 Characterization

The scanning electron microscope (SEM) images of the samples were obtained using a FEI Quanta 600 and transmission electron microscope (TEM) images were collected using a JEOL JEM 2010 and a FEI TECNAI G2 F20 FE-TEM. Fourier transform infrared spectra (FT-IR) of the samples were obtained using a Shimadzu IR Prestige attenuated total reflectance Fourier transform infrared (ATR-FTIR) spectrometer in range 3200 – 650 cm^{-1} . Raman spectroscopy analysis was conducted by Horiba Jobin-Yvon LabRam Raman confocal microscope with a 10 x objective and 632.8 nm excitation wavelength at room temperature. Laser power was set to 1.91 mW in order to avoid heat-induced damage to the sample. The pore size distribution of sample was estimated from analysis of SEM images using ImageJ 1.45s software.

3.2.4 Mechanical properties characterization

The compression tests were conducted using home-made mechanical properties measurement system with 50-lb. load cell (AL-101NH, AnyLoad) and two flat surface stages (top and bottom). Cylindrical CNT and composite aerogel samples with diameter of half inch were used for testing. The stress-strain curves (σ - ϵ curves) were measured at a strain rate of 40 mm min^{-1} and a 3% prestrain to make a uniform flat contact between compression stage and sample. The 10,000-cycle fatigue compressibility test was conducted by measuring stress (σ) versus 60% strain (ϵ) at strain rate of 400 mm min^{-1} with a 3% prestrain.

3.2.5 Electrical properties and thermal conductivity measurement

The compressibility-dependent electrical properties of composite aerogel were measured using a two-probe method. We attached aluminum foil as electrical wire leads to the flat surfaces of the sample with silver paste, and sample was loaded on the instrument with a 3% prestrain. A B&K digital multimeter was used to measure the resistance of composite aerogel as a function of strain. The thermal conductivity was measured by Thermal diffusivity system (FlashLine-3000, TA Instruments)

3.3 Results and Discussion

3.3.1 Fabrication and structural features of nanocomposites

We synthesized the carbon nanotubes sponge by the chemical vapor deposition (CVD) method reported by us previously.[79] Our carbon nanotubes have sponge-like porous structures with arbitrarily oriented and entangled CNT. The CNT sponge replicated the cylinder shape of a quartz tube as shown in figure 18a. The CNT sponge length was controlled by reaction time, and ~30 min reaction produced approximately 80~90 mm long cylindrical sponge. Scanning electron microscope (SEM) image of pristine CNT sponge displays porous CNT structures as shown in a figure 17b. The density of the CNT sponge was 25.5 mg cm^{-3} and porosity is $> 98.6\%$, respectively.

We fabricated CNT-PDMS composite aerogel using microwave heating. Carbon materials are excellent absorbents of microwave radiation, as a result they generate heat easily[65-67]. Due to this special characteristic of carbon materials, we expected carbon nanotubes to generate enough heat under microwave irradiation for the formation of polymer layer on carbon nanotubes. Therefore, we designed the microwave heating process for the fabrication of CNT-PDMS composite aerogel. Before the fabrication of sponge-type nanocomposite, we conducted the confirmatory experiment of the formation of CNT-polymer composite aerogel by microwave irradiation (figure 16). Figure 17c-f shows a SEM images of PDMS coated CNT after microwave irradiation for 5 seconds. PDMS is coated on CNT wall along the length of the CNT. This phenomenon can be

described by a rapid increasing temperature of CNT, which cause the solidification of PDMS on CNT. Therefore, figure 17 is clear evidence that CNT generate a lot of heat under the microwave radiation in a very short time since CNT are excellent absorbents of microwave radiation.

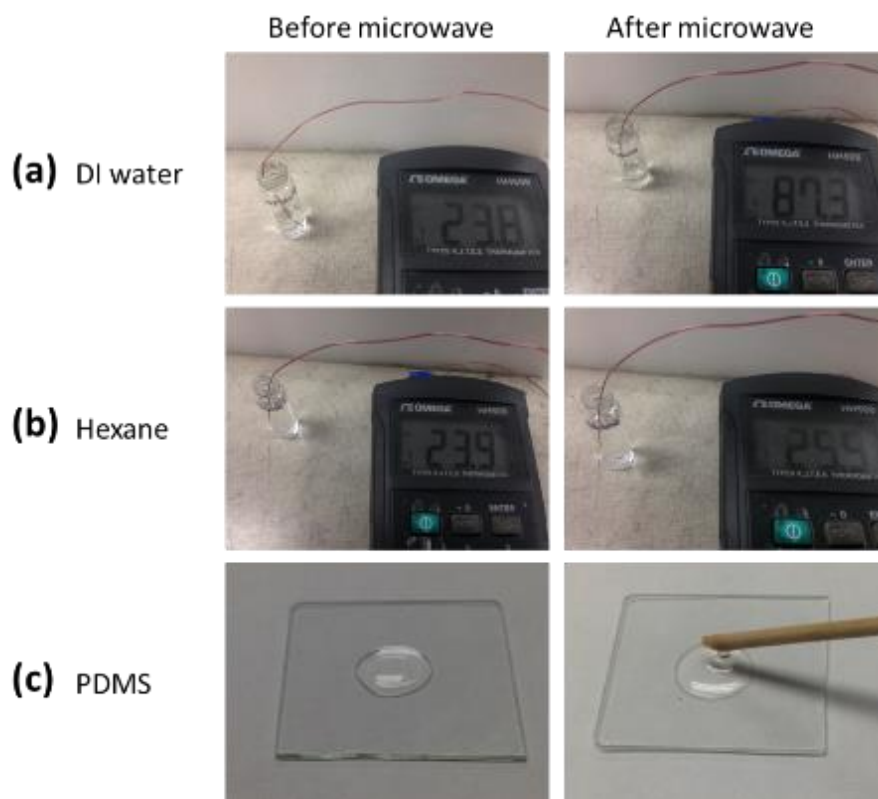


Figure 16. The microwave heating effect for polar and nonpolar materials. (a) DI water, (b) Hexane, and (c) PDMS. The photographs show the temperature different between before microwave and after microwave. The images indicate hexane and PDMS didn't absorb microwaves.

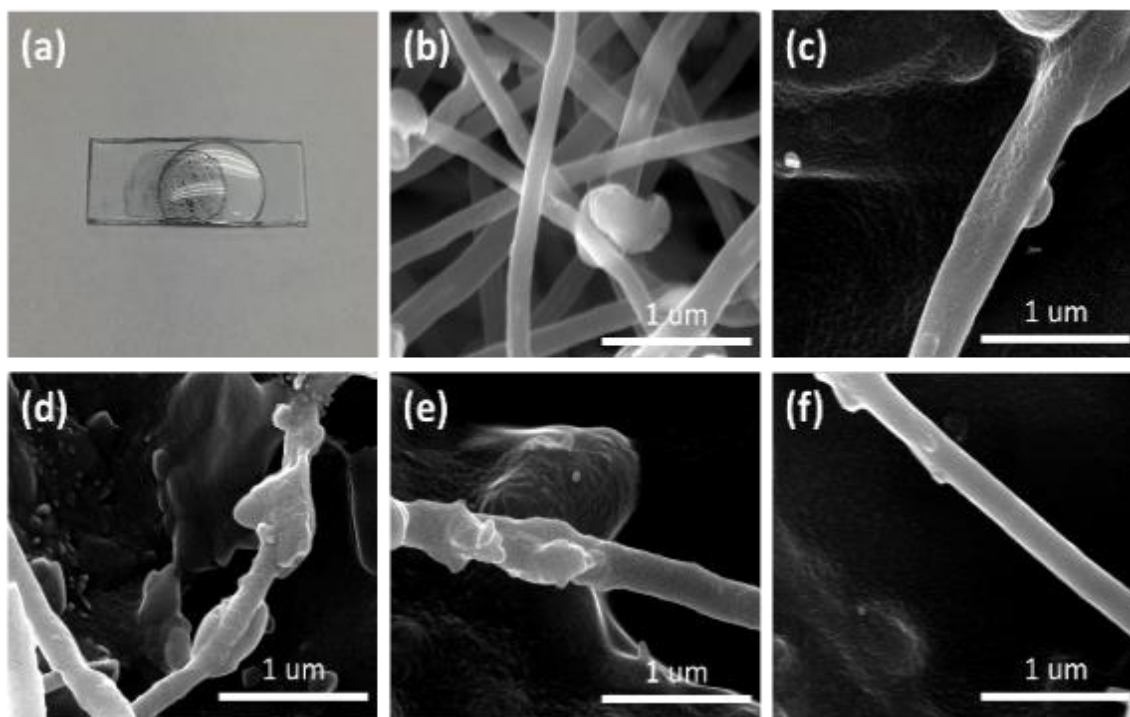


Figure 17. The curing PDMS polymer on carbon nanotubes sponge. (a) Photograph shows the PDMS solution drops onto CNT. (b) SEM image of pristine CNT sponge (c-f) SEM images of CNT-PDMS nanocomposite after microwave irradiation.

Based on the confirmatory experiment, we designed a simple fabrication process of composite aerogel. Figure 18a shows the fabrication process of the composite aerogel. The CNT sponge was soaked in a PDMS-hexane mixture solution in order to make a very thin uniform PDMS layer on CNT wall. We used hexane as solvent since hexane is a high-solubility solvent for PDMS[132]. The nanocomposite was exposed to microwave radiation for 3 seconds and then repeat 5 times for making a very thin PDMS layer. The

nanometer-thickness cured PDMS region is formed around CNT as a result of the dissipation of heat from CNT to PDMS. Although thermal conductivity of CNT is higher than that of PDMS (the reported values of CNT are $200 \sim 3000 \text{ W m}^{-1} \text{ K}^{-1}$ [133-135], which is much higher than that of PDMS, $0.13 \sim 0.2 \text{ W m}^{-1} \text{ K}^{-1}$ [136, 137]), heat dissipation happens by conduction and radiation from CNT to PDMS[138]. In addition, the temperature does not increase the decomposition temperature of polymer since the thermal resistance between CNT and PDMS makes a lower heating rate, so we can obtain a nanometer-sized PDMS layer on CNT wall by microwave radiation. Figure 18b and c show SEM images of the CNT-PDMS composite structure and its transmission electron microscope (TEM) images (figure 18d and e) show that CNT walls are composed of multiple graphitic layers and a $\sim 3\text{-nm}$ -thick PDMS layer was formed on the surface of CNT. In addition, the formation of junction between neighboring CNT might come from PDMS coating, as shown in figure 18c. PDMS coating can make a strong bonding between neighboring CNT and the bonding stability between neighboring CNT may affect the compression stability of the CNT-PDMS composite aerogel. The density of the CNT-PDMS composite aerogel was 29.4 mg cm^{-3} and porosity is $> 98.2\%$, respectively. Since the fabrication process in our methodology is very simple and faster process compared to other type of aerogel fabrication processes[62, 139], scaling up the fabrication of nanocomposite aerogel will be possible.

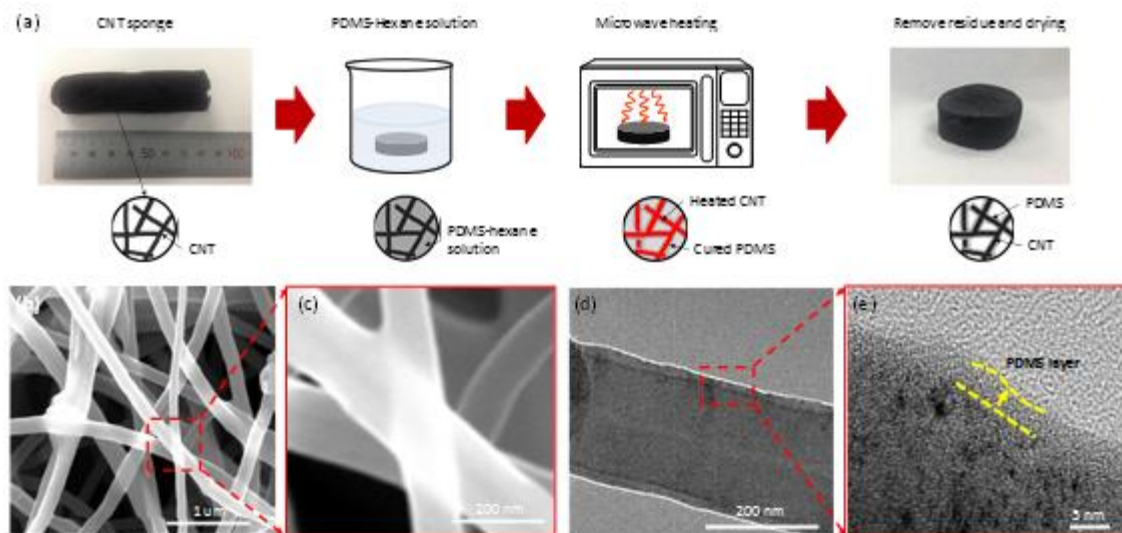


Figure 18. Fabrication and microstructure of CNT-PDMS composite aerogel. (a) Schematic of synthesis steps for making CNT-PDMS composite aerogel (b,c) SEM image of a 0.5 vol% PDMS nanocomposite sponge structure (d,e) TEM images of a 0.5 vol% PDMS composite aerogel structure, showing the structure of nanocomposite which has a very thin PDMS layer on the graphitic wall of carbon nanotubes

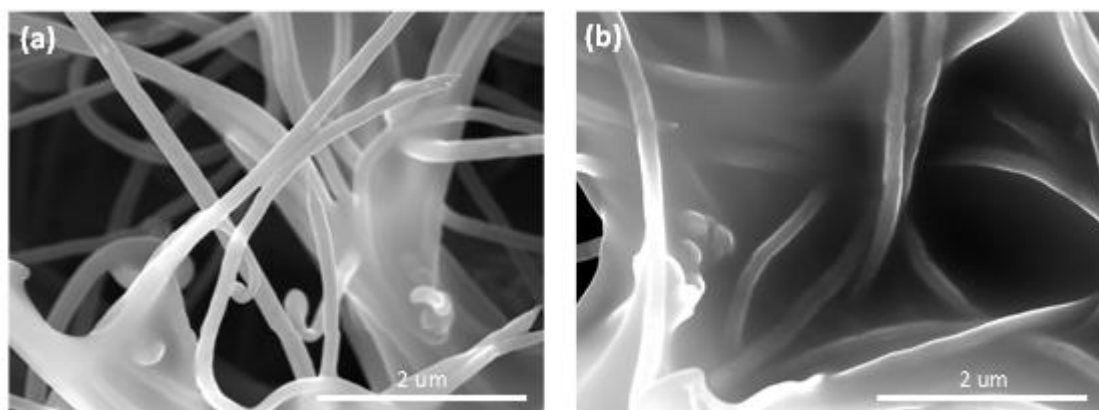


Figure 19. The SEM images of CNT-PDMS composite aerogel with different PDMS contents. (a) 3.2 vol% (b) 8 vol%

3.3.2 Characterization of composite aerogel structure

We further characterized the composite aerogel structure using FT-IR and Raman spectroscopy. Figure 20a shows the FTIR spectra of PDMS, CNT and the CNT-PDMS composite aerogel. In the FTIR spectrum of PDMS, the asymmetric peak that appears at 2961 cm^{-1} is owing to CH_3 stretching in CH_3 . The CH_3 deformation vibration peaks are observed in the range between 1400 and 1420 cm^{-1} and between 1200 and 1300 cm^{-1} . The Si-O-Si stretching multicomponent peaks appear in the range between 1000 and 1100 cm^{-1} and CH_3 rocking peaks in Si- CH_3 are observed at $750\sim 800\text{ cm}^{-1}$ and $850\sim 900\text{ cm}^{-1}$, respectively[140, 141]. Compared with PDMS, the peak shape of the CNT-PDMS composite aerogel in the range between 850 and 1100 cm^{-1} is changed due to the formation of a Si-C bond formed by interaction between CNT and PDMS[140, 142-144].

Raman spectroscopy has also been conducted to analyze the composite aerogel structure as shown in figure 20b. The intensity ratio (I_D/I_G) of D-band to G-band in the Raman spectra for CNT and the CNT-PDMS composite aerogel show that CNT have an intensity ratio of 1.01, respectively, demonstrating a relatively low crystallinity because of the defects on the CNT walls. It is possible to consider this structure is good for the fabrication of the CNT-PDMS composite aerogel because defects on CNT surface can promote the interaction between CNT and polymer[145]. The Raman spectra for the CNT-PDMS composite aerogel also show the characteristic peaks of carbon nanotubes at 1333 and 1589 cm^{-1} , respectively. It is possible to see the up-shift of G-band, 1589 cm^{-1} , which shows in CNT at 1583 cm^{-1} . This up-shift is associated with exerting a compression force

on carbon nanotubes by the polymer layer, changing the tangential motion of carbon nanotubes[146-148]. It indicates that there is an interfacial interaction between PDMS and CNT. Therefore, according to the Raman and FTIR spectra for composite aerogel, a polymer layer was formed on the surface of CNT by microwave radiation. This feature can also be observed in TEM images, as shown in figure 18d and e.

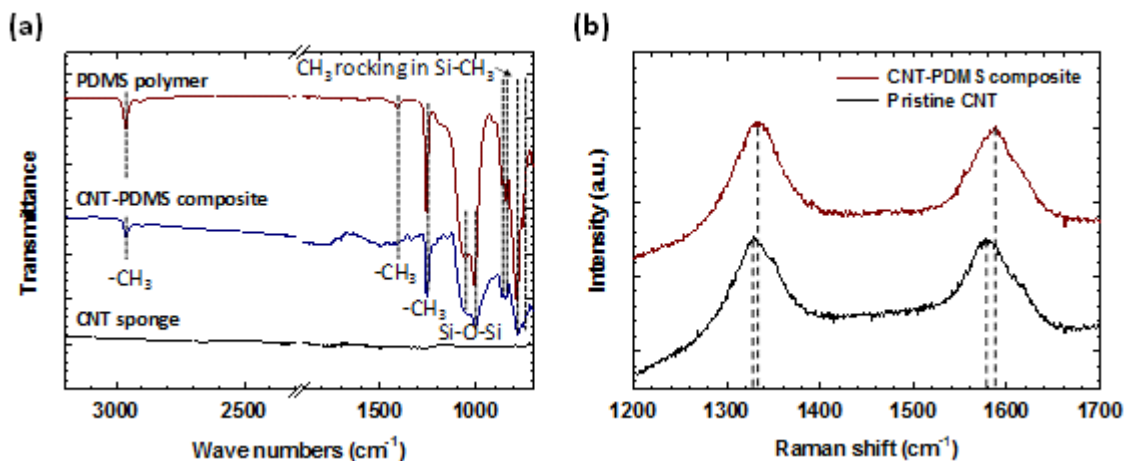


Figure 20. Characterization of CNT-PDMS composite aerogel structure. (a) Infrared spectra of CNT sponge, PDMS, and 0.5 vol% PDMS composite aerogel. (b) Raman spectra of CNT sponge and 0.5 vol% PDMS composite aerogel.

3.3.3 Mechanical properties of CNT-PDMS composite aerogel

The pristine CNT sponge has a large compressive stress reduction under the compression force as shown in figure 21 and figure 22c. To improve the elasticity, we designed the CNT-PDMS composite aerogel structure which has a thin polymer layer on CNT surface. Our hypothesis is that the CNT-polymer aerogel structure can show the outstanding mechanical properties and allow for a large deformation without fractures since hybridization with polymers is a typical method for the mechanical improvement of aerogel[30, 60]. The strong connection between neighboring CNT should assure the reversible elastic behavior without plastic deformation under compression. The composite aerogel can stand a compressive strain (ϵ) as high as 60% and recover its original shape after the release of the stress (σ), as shown in figure 22a and b.

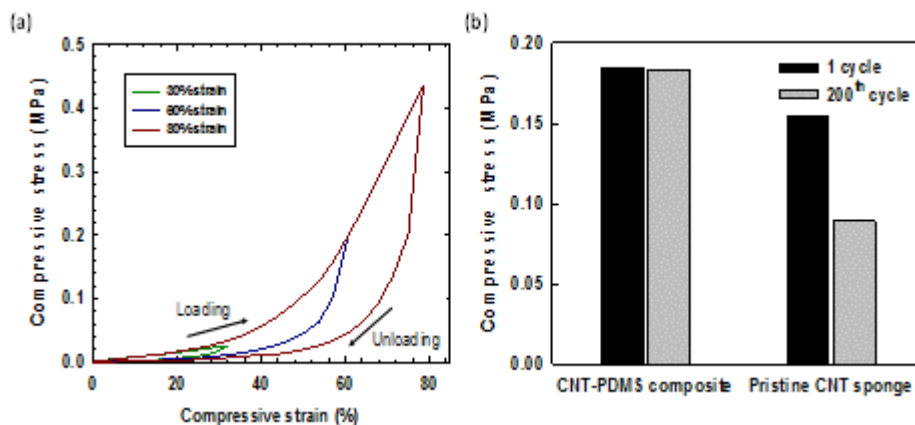


Figure 21. Compressive mechanical property of CNT-PDMS composite aerogel (a) Compressive stress-strain curves of CNT-PDMS composite aerogel at different set strains of 30, 60, and 80%, respectively. (b) Maximum compressive stress of CNT-PDMS composite aerogel and pristine CNT sponge at 60% strain. The black and grey bars represent the first and 200th cycle during compressive test.

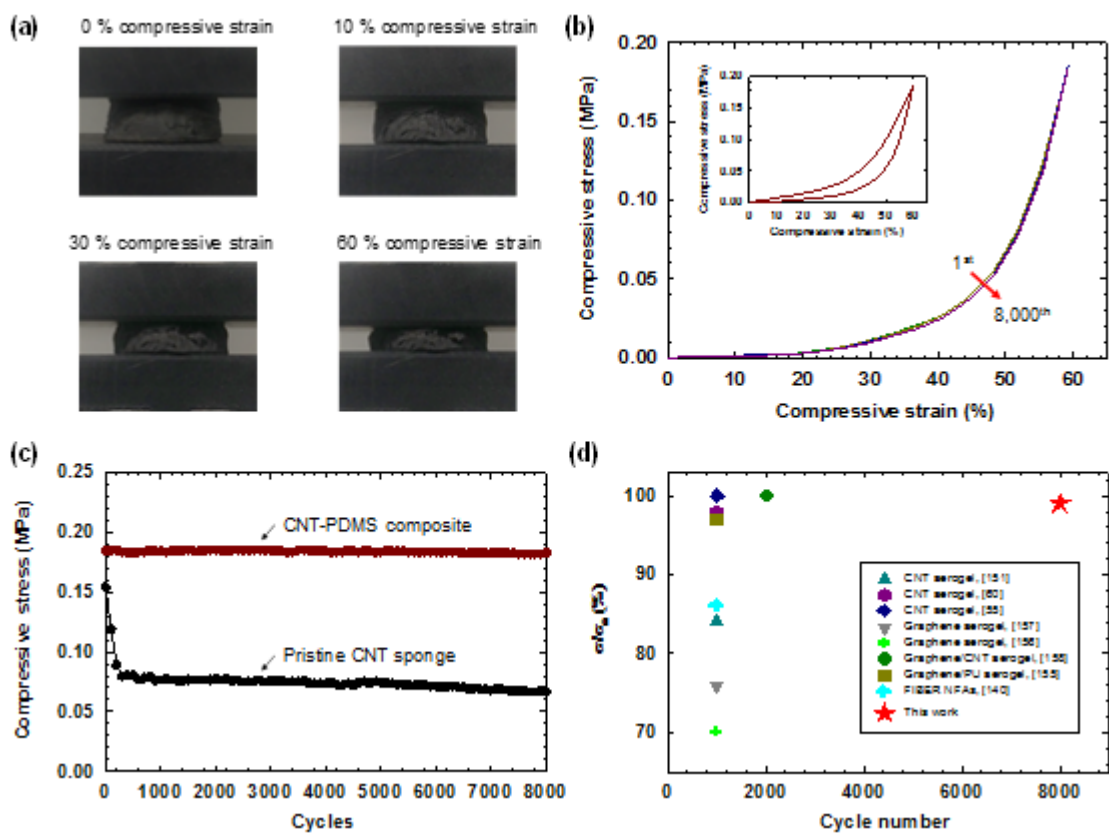


Figure 22. Mechanical properties of CNT-PDMS composite aerogel. (a) The photographs of the CNT-PDMS composite sponge at the different strains in the first compression cycle. (b) Compressive stress history of CNT-PDMS composite aerogel for 8,000 cycles at 60% compressive strain. (c) Maximum compressive stress of CNT-PDMS composite aerogel and pristine CNT sponge for 8,000 cycles at 60% strain. (d) Comparison of the compressive mechanical stability of CNT-PDMS composite aerogel and other materials. Note that the relative compressive stress of other materials would be different with different densities and we chose the best performance value from literatures.

Figure 22b shows the compressive stress-strain curve for 0.5 vol% PDMS composite aerogel at 60% as the maximum strain. We obtain a compressive strength 0.184 MPa at 60% compressive strain, which is much larger than other aerogel materials [53, 54, 149-151]. The CNT-PDMS composite aerogel can be compressed to more than 60% volume reduction because of high porosity and structural flexibility. The compressibility of nanocomposite can be visually indicated by the images in figure 22a, that clearly demonstrates the variations of sample height at different strain. While a pristine CNT sponge showed plastic deformation under compressive stress, the CNT-PDMS composite aerogel showed excellent structural stability (as shown in figure 22c), with almost recovery from large compressive strain (60%) because of strong junction between neighboring CNT by PDMS coating, as shown in figure 18b ~ e. The CNT-PDMS composite aerogel recovers to its original height after the release of the stress without measurable change in diameter, as shown in figure 22a and b. It is a similar result of the previous report that polymer composite aerogels demonstrate outstanding elastomeric behavior[30, 152, 153].

The CNT-PDMS composite aerogel was subjected to a cyclic fatigue compressibility test with 8,000 fatigue cycles at ε of 60%, and it showed no significant decrease in maximum stress (1% at 8,000th), which is extremely lower than pristine CNT sponge (43% at 200th), as shown in figure 22b and c. In comparison, other carbon based aerogels show a degradation in compressive strength of ~ 30% after 1,000 compressive cycles[54, 59, 139, 149, 150, 154-157], as shown in figure 3d and table 5. According to

the result, our aerogel can show the outstanding mechanical properties by coating PDMS layer on CNT.

3.3.4 Thermal insulation and electric properties of CNT-PDMS composite aerogel

Figure 23b shows thermal conductivity values of composite aerogel with different PDMS contents. The 0.5 vol% PDMS composite aerogel with a density of 29.4 mg cm^{-3} showed an outstanding thermal conductivity of $26 \text{ mW m}^{-1} \text{ K}^{-1}$, which is similar to that of pristine CNT sponge with a density of 25.6 mg cm^{-3} and that of air at ambient condition ($23 \text{ mW m}^{-1} \text{ K}^{-1}$). Typical aerogels are well-known thermal insulation materials with extremely low thermal conductivity due to high porosity[129, 158]. According to the result, thermal conductivity was increased when PDMS content was increased due to the decrease of the porosity. In addition, thermal conductivity values of CNT-PDMS composite aerogel had changed little after 1,000 cycles, it indicates that a nanometer-size polymer layer on CNT enhance the mechanical strength and compressibility without affecting the increase in thermal conductivity, as shown in figure 23a. According to the result, our composite aerogel shows ultra-low thermal conductivity with high mechanical strength and resilience, suggesting its use as promising thermal insulation materials with high mechanical properties in a broad range of applications.

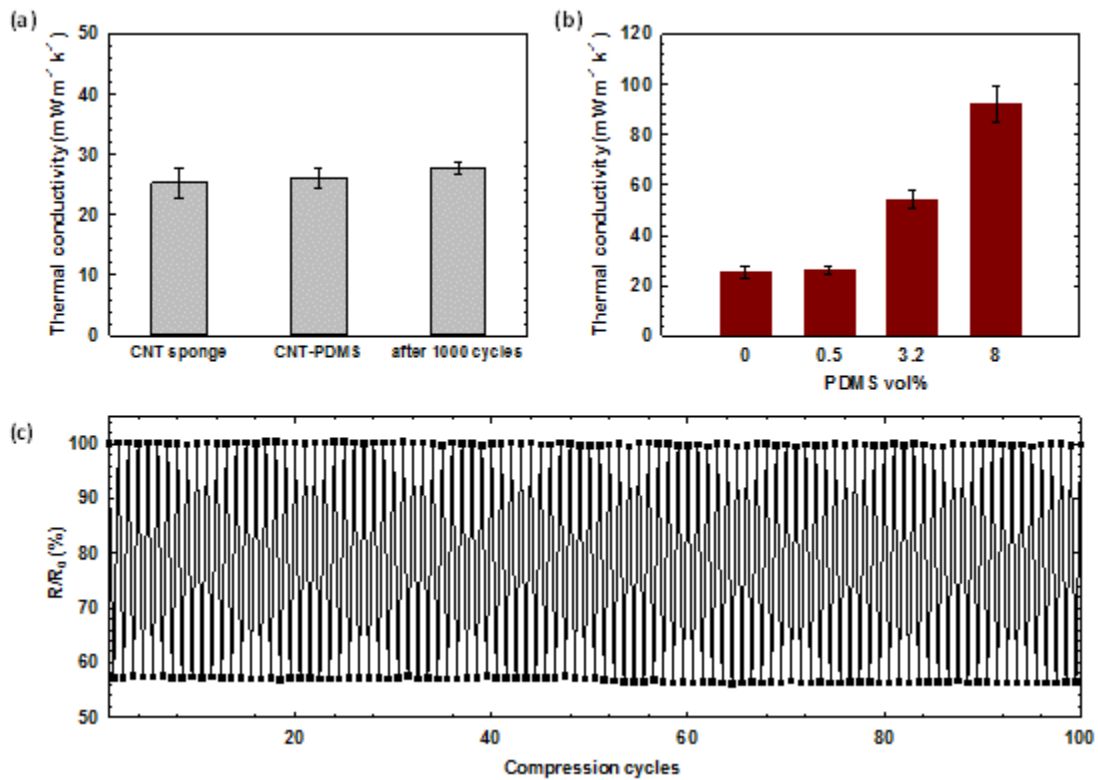


Figure 23. Thermal insulation and electric properties of CNT-PDMS composite aerogel. (a) Thermal conductivity values of pristine CNT sponge, CNT-PDMS composite aerogel, and after 1,000 cyclic compressive test with 60% strain. (b) Thermal conductivity values and porosity of CNT-PDMS composite aerogel with different PDMS contents. (c) R/R_0 of the CNT-PDMS composite aerogel when repeatedly compressed ($\epsilon=50\%$) for 100 cycles.

The thermal conductivity value of the composite aerogel is related to the thermal properties of the components and the structure of composite aerogel[159]. The average diameter of the composite aerogel pores was estimated from analysis of SEM cross-

section images using ImageJ 1.45s software (figure 24). The gas contribution to thermal conductivity can be estimated according to

$$\kappa_g = \frac{\kappa_{g0}\Pi}{1+2\beta K_n} \quad (5)$$

where Π is the porosity, κ_{g0} is the thermal conductivity of gas, $\beta \approx 2$ for the parameter of energy transfer between gas molecules and solid structure[159]. The Knudsen number, K_n , is

$$K_n = \frac{l_g}{\delta} \quad (6)$$

where l_g is the mean free path of a gas molecule and δ describes the pore diameter. We estimated the gas conductivity with composite aerogel that the gas thermal conductivity κ_g remains below the value of κ_{g0} .

The nano-sized solid components also have an interfacial thermal resistance, as known as the Kapitza resistance, which leads to decrease the thermal conductivity of solid components[62, 160]. The effective solid conductivity, κ_{sol}^* , of individual solid components of composite aerogel uses

$$\kappa_{sol}^* = \frac{\kappa_{sol}}{1+\kappa_{sol}\frac{R_k}{d}} \quad (7)$$

where d is the diameter of CNT and PDMS layer, and κ_{sol} is the thermal conductivity of individual components. The R_k values of components of composite aerogel were taken from literatures[160, 161](see table 4 for a detailed description). We calculated the thermal conductivity of solid components using equation (3), suggesting that composite structure can reduce κ_{sol}^* from $\sim 1,200 \text{ mW m}^{-1} \text{ K}^{-1}$ for bulk material with same

composition as composite aerogel to below $10 \text{ mW m}^{-1}\text{K}^{-1}$ for the composite aerogel since phonon scattering[160].

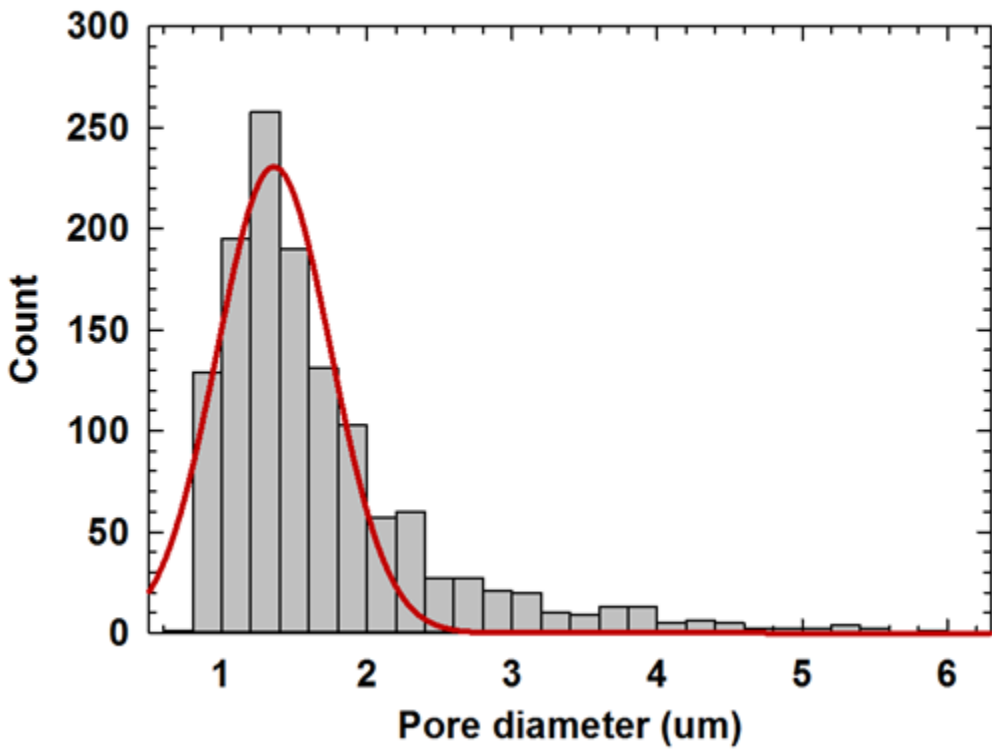


Figure 24. Pore size distribution of CNT-PDMS composite aerogel.

Table 4. Estimation of gas and solid thermal conductivity of nanocomposite aerogel

Gas component	K_g (W m ⁻¹ K ⁻¹)	Π	β	Kn		K_g (W m ⁻¹ K ⁻¹)
				l_m (nm)	δ (μm)	
Ar	0.0178 [162]	0.982	2 [163]	75	1.69	0.0148

Solid component	K_{sol} (W m ⁻¹ K ⁻¹)	d (nm)	R_K (x10 ⁻⁸ m ² K W ⁻¹)	k_s^* (W m ⁻¹ K ⁻¹)
PDMS	0.25 [165]	3	8.3 [160]	0.032

The relative electrical resistance (R/R_0) of CNT-PDMS composite aerogel was also relatively constant over 100 cycles, as shown in figure 23c, representing the promising structural stability. In addition, figure 25 shows the electrical resistance of the CNT-PDMS composite aerogel as a function of compressive strain, which showed the initial electrical conductivity of 20 S m⁻¹ without strain. The relative electrical resistance (R/R_0) decreased by approximately 55% with an increase in strain to 60% and recovered like the initial electrical resistance during the unloading. The compressive stress made plenty of new electrical contacts, and added to the existing conduction paths through the composite aerogel, lastly decreased the electrical resistance. When the compressive stress was removed, new electrical contacts disappeared, the composite aerogel

recovered to the initial electrical resistance and sprang back to its original shape. Therefore, these results support the use of CNT-PDMS composite aerogel as pressure sensor and flexible electrodes for various applications.

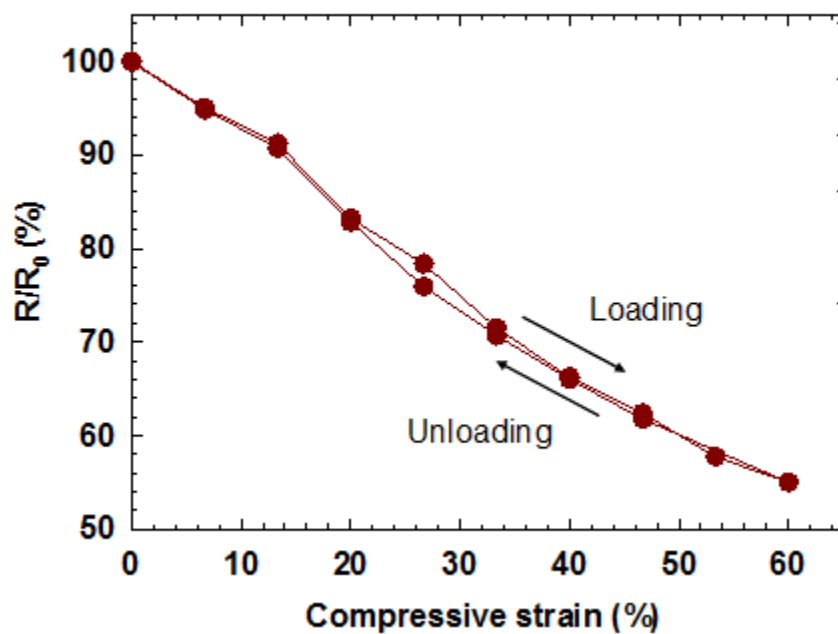


Figure 25. R/R_0 of the CNT-PDMS composite aerogel as a function of compressive strain ($\epsilon=60\%$)

Table 5. Comparison of the materials properties of CNT-PDMS nanocomposite and other materials*

* Note that the properties of other materials would be different with different densities and we chose the best performance as their reported value.

Materials	Compressive stress (MPa)	Cyclic compression stability	Electrical conductivity ($S m^{-1}$)	Thermal conductivity ($mW m^{-1} K^{-1}$)	Ref.
Carbon Aerogels	0.006 at 50% strain	88% of the original value at 1000 th cycles	0.6	Not reported	[156]
Carbon Nanotube Aerogel	0.004 at 60% strain	84% of the original value at 1000 th cycles	3.2	Not reported	[151]
Carbon Nanotube Sponge composite	0.028 at 60% strain	70% of the original value at 300 th cycles	58	Not reported	[54]
Carbon Nanotube Sponges	0.033 at 60% strain	100% of the original value at 1000 th cycles	Not reported	150	[55]
Cellulose nanofibers based composite foam	0.18 at 90% strain	Not reported	Not reported	15	[63]
Nanofibrous aerogels	0.011 at 60% strain	86% of the original value at 1000 th cycles	25	26	[140]
This work	0.26 at 60% strain	92% of the original value at 1000 th cycles	20	26	

3.4 Conclusions

In conclusion, we have shown that the facile and quick process for the scalable production of super resilient with multifunctionality CNT-PDMS composite aerogel using microwave heating. The microwave heating process leads to a quick reaction and allows for the uniform polymer layer on CNT. The nanometer-thickness PDMS layer coated CNT sponge shows high mechanical strength (0.184 MPa), compressibility, thermal insulation ($26 \text{ mW m}^{-1} \text{ K}^{-1}$) and elasticity-dependent electric conduction. Although further studies are needed to optimize the processing to adjust this process for many applications, we believe that super resilient with multifunctionality CNT-PDMS composite aerogel will expose the chance for many applications, such as heat insulator, pressure sensor, dampers and flexible electrodes.

CHAPTER IV

SUMMARY AND CONCLUSIONS

4.1 One-step synthesis of nitrogen-iron coordinated carbon nanotube catalysts for oxygen reduction reaction

Prohibitively expensive precious metal catalysts for oxygen reduction reaction (ORR) have been one of the major hurdles in a wide use of electrochemical cells. Recent significant efforts to develop precious metal free catalysts have resulted in excellent catalytic activities. The electrochemical performances of nanostructured carbon with transition metals and nitrogen catalysts in recently published reports were comparable to those of Pt-based catalysts, but the high manufacturing costs due to complicated synthesis processes negate the benefit of eliminating the precious metal catalysts, which have time-consuming polymerization processes and additional leaching steps were necessary to remove inactive materials. Moreover, detailed analysis about catalytically active sites and the role of each element in these high-performance catalysts containing nanomaterials for large surface areas are often lacking. We synthesized nitrogen and iron doped CNTs for oxygen reduction reaction by one-step synthesis. Fe-A/P-CNT showed significantly high electrocatalytic activity and long-term stability (up to 30,000 cycles) comparable to those of Pt based commercial catalysts. Our nitrogen-iron coordinated carbon nanotube catalysts without precious metals were grown a one-step synthesis method for scale-up

manufacturing in the future, and showed superior and/or comparable oxygen reduction reaction performance with greatly improved long term stability compared to previously reported non-precious metal based catalysts. Furthermore, we identified report the coordination of nitrogen and iron forming oxygen reduction reaction sites could contribute to the significantly high performance. In addition, we identified that the coordination of nitrogen and iron in carbon based nanostructures played a key role in achieving the high ORR performances by comparing catalytic activities of different CNT catalysts synthesized with/without iron and/or nitrogen from aniline and pyridine. We anticipate further study in our one-step synthesis process may result in scalable mass production of non-precious metal catalysts for a broad range of electrochemical cells. Our catalysts show excellent long-term stability and onset ORR potential comparable to those of other precious metal free catalysts, and the maximum limiting current density from our catalysts is larger than that of the Pt-based catalysts.

4.2 Ultra-resilient carbon nanotube composites aerogel with thermal insulation and electrical properties by microwave irradiation

The demand for aerogels with highly compressible and resilient being increased in a wide range of applications from bioengineering to aerospace. Carbon nanotubes provide a combination of compressibility and resilient, and these excellent mechanical properties have been desirable in carbon-based aerogels. Nevertheless, carbon-based aerogels

suffer significant plastic deformation and compressive strength reduction during the repeated strain. Furthermore, the fabrication of such aerogels has shown severely challenging and complicated. Here, we report the facile and quick process for the scalable production of super resilient CNT-PDMS sponge nanocomposite with ultra-low thermal conductivity and high electrical properties by microwave heating. The nanometer-thickness PDMS layer coated CNT sponge shows high mechanical strength (0.184 MPa), compressibility, thermal insulation ($26 \text{ mW m}^{-1} \text{ K}^{-1}$) and elasticity-dependent electric conduction. The successful fabrication of super resilient CNT-PDMS sponge nanocomposite with multifunctionality will expose the chance for many applications.

REFERENCES

- [1] R.H. Baughman, A.A. Zakhidov, W.A. de Heer, Carbon nanotubes--the route toward applications, *Science*, 297 (2002) 787-792.
- [2] J.M. Schnorr, T.M. Swager, Emerging applications of carbon nanotubes†, *Chemistry of Materials*, 23 (2010) 646-657.
- [3] E.T. Thostenson, Z. Ren, T.-W. Chou, Advances in the science and technology of carbon nanotubes and their composites: a review, *Composites Science and Technology*, 61 (2001) 1899-1912.
- [4] P. Ayala, R. Arenal, M. Rummeli, A. Rubio, T. Pichler, The doping of carbon nanotubes with nitrogen and their potential applications, *Carbon*, 48 (2010) 575-586.
- [5] S. Iijima, Direct observation of the tetrahedral bonding in graphitized carbon black by high resolution electron microscopy, *Journal of Crystal Growth*, 50 (1980) 675-683.
- [6] A. Oberlin, M. Endo, T. Koyama, High resolution electron microscope observations of graphitized carbon fibers, *Carbon*, 14 (1976) 133-135.
- [7] A. Oberlin, M. Endo, T. Koyama, Filamentous growth of carbon through benzene decomposition, *Journal of Crystal Growth*, 32 (1976) 335-349.
- [8] S. Iijima, Helical microtubules of graphitic carbon, *Nature*, 354 (1991) 56-58.
- [9] M.S. Dresselhaus, P. Avouris, Introduction to Carbon Materials Research, in: M.S. Dresselhaus, G. Dresselhaus, P. Avouris (Eds.) *Carbon Nanotubes: Synthesis, Structure,*

Properties, and Applications, Springer Berlin Heidelberg, Berlin, Heidelberg, 2001, pp. 1-9.

[10] H.W. Kroto, J.R. Heath, S.C. O'Brien, R.F. Curl, R.E. Smalley, C60: Buckminsterfullerene, *Nature*, 318 (1985) 162-163.

[11] S. Iijima, T. Ichihashi, Single-shell carbon nanotubes of 1-nm diameter, *Nature*, 363 (1993) 603-605.

[12] D.S. Bethune, C.H. Klang, M.S. de Vries, G. Gorman, R. Savoy, J. Vazquez, R. Beyers, Cobalt-catalysed growth of carbon nanotubes with single-atomic-layer walls, *Nature*, 363 (1993) 605-607.

[13] M.S. Dresselhaus, G. Dresselhaus, R. Saito, Carbon fibers based on C60 and their symmetry, *Physical Review B*, 45 (1992) 6234-6242.

[14] J.W. Mintmire, B.I. Dunlap, C.T. White, Are fullerene tubules metallic?, *Physical Review Letters*, 68 (1992) 631-634.

[15] N. Hamada, S.-i. Sawada, A. Oshiyama, New one-dimensional conductors: Graphitic microtubules, *Physical Review Letters*, 68 (1992) 1579-1581.

[16] J.W.G. Wilder, L.C. Venema, A.G. Rinzler, R.E. Smalley, C. Dekker, Electronic structure of atomically resolved carbon nanotubes, *Nature*, 391 (1998) 59-62.

[17] T.W. Odom, J.-L. Huang, P. Kim, C.M. Lieber, Atomic structure and electronic properties of single-walled carbon nanotubes, *Nature*, 391 (1998) 62-64.

- [18] A. Thess, R. Lee, P. Nikolaev, H. Dai, P. Petit, J. Robert, C. Xu, Y.H. Lee, S.G. Kim, A.G. Rinzler, D.T. Colbert, G.E. Scuseria, D. Tománek, J.E. Fischer, R.E. Smalley, Crystalline ropes of metallic carbon nanotubes, *Science*, 273 (1996) 483-487.
- [19] C.H. Olk, J.P. Heremans, Scanning tunneling spectroscopy of carbon nanotubes, *Journal of Materials Research*, 9 (2011) 259-262.
- [20] R. Saito, G. Dresselhaus, M.S. Dresselhaus, *Physical Properties of Carbon Nanotubes*, World Scientific, 1998.
- [21] M.S. Dresselhaus, G. Dresselhaus, P.C. Eklund, *Science of fullerenes and carbon nanotubes: their properties and applications*, Academic Press, 1996.
- [22] J. Sloan, M. Terrones, S. Nufer, S. Friedrichs, S.R. Bailey, H.-G. Woo, M. Rühle, J.L. Hutchison, M.L. Green, Metastable one-dimensional AgCl_{1-x} I x solid-solution wurzite “Tunnel” crystals formed within single-walled carbon nanotubes, *Journal of the American Chemical Society*, 124 (2002) 2116-2117.
- [23] W. Chen, *Doped Nanomaterials and Nanodevices: Luminescence and applications*, American Scientific Publishers, 2010.
- [24] M. Terrones, A.G. Souza Filho, A.M. Rao, *Doped carbon nanotubes: synthesis, characterization and applications*, *Carbon Nanotubes*, Springer, 2007, pp. 531-566.
- [25] L. Feng, Y. Chen, L. Chen, Easy-to-operate and low-temperature synthesis of gram-scale nitrogen-doped graphene and its application as cathode catalyst in microbial fuel cells, *ACS Nano*, 5 (2011) 9611-9618.

- [26] L. Qu, Y. Liu, J.-B. Baek, L. Dai, Nitrogen-doped graphene as efficient metal-free electrocatalyst for oxygen reduction in fuel cells, *ACS Nano*, 4 (2010) 1321-1326.
- [27] B. Arash, Q. Wang, V.K. Varadan, Mechanical properties of carbon nanotube/polymer composites, *Scientific Reports*, 4 (2014) 6479.
- [28] D.R. Askeland, *Composite Materials, The Science and Engineering of Materials*, Springer US, Boston, MA, 1996, pp. 549-594.
- [29] K.-t. Lau, C. Gu, D. Hui, A critical review on nanotube and nanotube/nanoclay related polymer composite materials, *Composites Part B: Engineering*, 37 (2006) 425-436.
- [30] S. Ye, J. Feng, P. Wu, Highly elastic graphene oxide-epoxy composite aerogels via simple freeze-drying and subsequent routine curing, *Journal of Materials Chemistry A*, 1 (2013) 3495-3502.
- [31] P.P. Mukherjee, Q. Kang, C.-Y. Wang, Pore-scale modeling of two-phase transport in polymer electrolyte fuel cells-progress and perspective, *Energy & Environmental Science*, 4 (2011) 346-369.
- [32] H.A. Gasteiger, S.S. Kocha, B. Sompalli, F.T. Wagner, Activity benchmarks and requirements for Pt, Pt-alloy, and non-Pt oxygen reduction catalysts for PEMFCs, *Applied Catalysis B: Environmental*, 56 (2005) 9-35.
- [33] F. Jaouen, E. Proietti, M. Lefevre, R. Chenitz, J.P. Dodelet, G. Wu, H.T. Chung, C.M. Johnston, P. Zelenay, Recent advances in non-precious metal catalysis for oxygen-

reduction reaction in polymer electrolyte fuel cells, *Energy & Environmental Science*, 4 (2011) 114-130.

[34] G. Wu, C.M. Johnston, N.H. Mack, K. Artyushkova, M. Ferrandon, M. Nelson, J.S. Lezama-Pacheco, S.D. Conradson, K.L. More, D.J. Myers, P. Zelenay, Synthesis-structure-performance correlation for polyaniline-Me-C non-precious metal cathode catalysts for oxygen reduction in fuel cells, *Journal of Materials Chemistry*, 21 (2011) 11392-11405.

[35] R. Bashyam, P. Zelenay, A class of non-precious metal composite catalysts for fuel cells, *Nature*, 443 (2006) 63-66.

[36] M. Lefevre, E. Proietti, F. Jaouen, J.P. Dodelet, Iron-based catalysts with improved oxygen reduction activity in polymer electrolyte fuel cells, *Science*, 324 (2009) 71-74.

[37] E. Proietti, F. Jaouen, M. Lefevre, N. Larouche, J. Tian, J. Herranz, J.P. Dodelet, Iron-based cathode catalyst with enhanced power density in polymer electrolyte membrane fuel cells, *Nature Communications*, 2 (2011).

[38] G. Wu, K.L. More, C.M. Johnston, P. Zelenay, High-performance electrocatalysts for oxygen reduction derived from polyaniline, iron, and cobalt, *Science*, 332 (2011) 443-447.

[39] S. J., Cost Analyses of Fuel Cell Stacks/Systems, in: D.o. Energy (Ed.) 2010 Annual Progress Report V. Fuel Cells, 2010.

- [40] K. Gong, F. Du, Z. Xia, M. Durstock, L. Dai, Nitrogen-doped carbon nanotube arrays with high electrocatalytic activity for oxygen reduction, *Science*, 323 (2009) 760-764.
- [41] Y. Shao, J. Sui, G. Yin, Y. Gao, Nitrogen-doped carbon nanostructures and their composites as catalytic materials for proton exchange membrane fuel cell, *Applied Catalysis B: Environmental*, 79 (2008) 89-99.
- [42] W. Ding, Z.D. Wei, S.G. Chen, X.Q. Qi, T. Yang, J.S. Hu, D. Wang, L.J. Wan, S.F. Alvi, L. Li, Space-confinement-induced synthesis of pyridinic- and pyrrolic-nitrogen-doped graphene for the catalysis of oxygen reduction, *Angewandte Chemie International Edition*, 52 (2013) 11755-11759.
- [43] Y. Ito, H.J. Qiu, T. Fujita, Y. Tanabe, K. Tanigaki, M. Chen, Bicontinuous nanoporous N-doped graphene for the oxygen reduction reaction, *Advanced Materials*, (2014).
- [44] I. Hijazi, T. Bourgeteau, R. Cornut, A. Morozan, A. Filoramo, J. Leroy, V. Derycke, B. Jousset, S. Campidelli, Carbon nanotube-templated synthesis of covalent porphyrin network for oxygen reduction reaction, *Journal of the American Chemical Society*, 136 (2014) 6348-6354.
- [45] G. Nam, J. Park, S.T. Kim, D.B. Shin, N. Park, Y. Kim, J.S. Lee, J. Cho, Metal-free Ketjenblack incorporated nitrogen-doped carbon sheets derived from gelatin as oxygen reduction catalysts, *Nano Letters*, 14 (2014) 1870-1876.

- [46] D.M.S.n.a.D.G.Z. Dr. Horst Jahnke, Organic dyestuffs as catalysts for fuel cells, *Topics in Current Chemistry*, 61 (1976).
- [47] H. Alt, H. Binder, G. Sandstede, Mechanism of the electrocatalytic reduction of oxygen on metal chelates, *Journal of Catalysis*, 28 (1973) 8-19.
- [48] A. Ishihara, Y. Ohgi, K. Matsuzawa, S. Mitsushima, K.-i. Ota, Progress in non-precious metal oxide-based cathode for polymer electrolyte fuel cells, *Electrochimica Acta*, 55 (2010) 8005-8012.
- [49] E. HaoYu, S. Cheng, K. Scott, B. Logan, Microbial fuel cell performance with non-Pt cathode catalysts, *Journal of Power Sources*, 171 (2007) 275-281.
- [50] M. Bron, J. Radnik, M. Fieber-Erdmann, P. Bogdanoff, S. Fiechter, EXAFS, XPS and electrochemical studies on oxygen reduction catalysts obtained by heat treatment of iron phenanthroline complexes supported on high surface area carbon black, *Journal of Electroanalytical Chemistry*, 535 (2002) 113-119.
- [51] C.W.B. Bezerra, L. Zhang, K. Lee, H. Liu, A.L.B. Marques, E.P. Marques, H. Wang, J. Zhang, A review of Fe–N/C and Co–N/C catalysts for the oxygen reduction reaction, *Electrochimica Acta*, 53 (2008) 4937-4951.
- [52] Y. Li, W. Zhou, H. Wang, L. Xie, Y. Liang, F. Wei, J.C. Idrobo, S.J. Pennycook, H. Dai, An oxygen reduction electrocatalyst based on carbon nanotube-graphene complexes, *Nature Nanotechnology*, 7 (2012) 394-400.

- [53] X. Gui, A. Cao, J. Wei, H. Li, Y. Jia, Z. Li, L. Fan, K. Wang, H. Zhu, D. Wu, Soft, highly conductive nanotube sponges and composites with controlled compressibility, *ACS Nano*, 4 (2010) 2320-2326.
- [54] X. Gui, J. Wei, K. Wang, A. Cao, H. Zhu, Y. Jia, Q. Shu, D. Wu, Carbon nanotube sponges, *Advanced Materials*, 22 (2010) 617-621.
- [55] C. Yu, L. Shi, Z. Yao, D. Li, A. Majumdar, Thermal conductance and thermopower of an individual single-wall carbon nanotube, *Nano Letters*, 5 (2005) 1842-1846.
- [56] T.-Y. Choi, D. Poulikakos, J. Tharian, U. Sennhauser, Measurement of the thermal conductivity of individual carbon nanotubes by the four-point three- ω method, *Nano Letters*, 6 (2006) 1589-1593.
- [57] D.N. Futaba, K. Hata, T. Yamada, T. Hiraoka, Y. Hayamizu, Y. Kakudate, O. Tanaike, H. Hatori, M. Yumura, S. Iijima, Shape-engineerable and highly densely packed single-walled carbon nanotubes and their application as super-capacitor electrodes, *Nature Materials*, 5 (2006) 987-994.
- [58] J. Biener, M. Stadermann, M. Suss, M.A. Worsley, M.M. Biener, K.A. Rose, T.F. Baumann, Advanced carbon aerogels for energy applications, *Energy & Environmental Science*, 4 (2011) 656-667.
- [59] Z. Dai, L. Liu, X. Qi, J. Kuang, Y. Wei, H. Zhu, Z. Zhang, Three-dimensional sponges with super mechanical stability: Harnessing true elasticity of individual carbon nanotubes in macroscopic architectures, *Scientific Reports*, 6 (2016) 18930.

- [60] L. Zhang, Z. Wang, C. Xu, Y. Li, J. Gao, W. Wang, Y. Liu, High strength graphene oxide/polyvinyl alcohol composite hydrogels, *Journal of Materials Chemistry*, 21 (2011) 10399-10406.
- [61] J. Zhang, Y. Cao, J. Feng, P. Wu, Graphene-oxide-sheet-induced gelation of cellulose and promoted mechanical properties of composite aerogels, *The Journal of Physical Chemistry C*, 116 (2012) 8063-8068.
- [62] B. Wicklein, A. Kocjan, G. Salazar-Alvarez, F. Carosio, G. Camino, M. Antonietti, L. Bergström, Thermally insulating and fire-retardant lightweight anisotropic foams based on nanocellulose and graphene oxide, *Nature Nanotechnology*, 10 (2015) 277-283.
- [63] B.N. Nguyen, M.A.B. Meador, A. Medoro, V. Arendt, J. Randall, L. McCorkle, B. Shonkwiler, Elastic behavior of methyltrimethoxysilane based aerogels reinforced with tri-isocyanate, *ACS Applied Materials & Interfaces*, 2 (2010) 1430-1443.
- [64] K.H. Kim, M. Vural, M.F. Islam, Single-walled carbon nanotube aerogel-based elastic conductors, *Advanced Materials*, 23 (2011) 2865-2869.
- [65] J.A. Menéndez, A. Arenillas, B. Fidalgo, Y. Fernández, L. Zubizarreta, E.G. Calvo, J.M. Bermúdez, Microwave heating processes involving carbon materials, *Fuel Processing Technology*, 91 (2010) 1-8.
- [66] U.O. Méndez, O.V. Kharissova, M. Rodríguez, Synthesis and morphology of nanostructures via microwave heating, *Reviews on Advanced Materials Science*, 5 (2003) 398.

- [67] E. Vazquez, M. Prato, Carbon nanotubes and microwaves: interactions, responses, and applications, *ACS Nano*, 3 (2009) 3819-3824.
- [68] A.L. Higginbotham, P.G. Moloney, M.C. Waid, J.G. Duque, C. Kittrell, H.K. Schmidt, J.J. Stephenson, S. Arepalli, L.L. Yowell, J.M. Tour, Carbon nanotube composite curing through absorption of microwave radiation, *Composites Science and Technology*, 68 (2008) 3087-3092.
- [69] C.Y. Wang, T.H. Chen, S.C. Chang, T.S. Chin, S.Y. Cheng, Flexible field emitter made of carbon nanotubes microwave welded onto polymer substrates, *Applied Physics Letters*, 90 (2007) 103111.
- [70] T.J. Imholt, C.A. Dyke, B. Hasslacher, J.M. Perez, D.W. Price, J.A. Roberts, J.B. Scott, A. Wadhawan, Z. Ye, J.M. Tour, Nanotubes in microwave fields: Light emission, intense heat, outgassing, and reconstruction, *Chemistry of Materials*, 15 (2003) 3969-3970.
- [71] Z. Ye, W.D. Deering, A. Krokhin, J.A. Roberts, Microwave absorption by an array of carbon nanotubes: A phenomenological model, *Physical Review B*, 74 (2006) 075425.
- [72] K.E. Haque, Microwave energy for mineral treatment processes—a brief review, *International Journal of Mineral Processing*, 57 (1999) 1-24.
- [73] C.Y. Wang, T.H. Chen, S.C. Chang, S.Y. Cheng, T.S. Chin, Strong carbon-nanotube-polymer bonding by microwave irradiation, *Advanced Functional Materials*, 17 (2007) 1979-1983.

- [74] K.R. Paton, A.H. Windle, Efficient microwave energy absorption by carbon nanotubes, *Carbon*, 46 (2008) 1935-1941.
- [75] S. Vongpradubchai, P. Rattanadecho, The microwave processing of wood using a continuous microwave belt drier, *Chemical Engineering and Processing: Process Intensification*, 48 (2009) 997-1003.
- [76] Z. Huang, M. Gotoh, Y. Hirose, Improving sinterability of ceramics using hybrid microwave heating, *Journal of Materials Processing Technology*, 209 (2009) 2446-2452.
- [77] N. Makul, P. Rattanadecho, Microwave pre-curing of natural rubber-compounding using a rectangular wave guide, *International Communications in Heat and Mass Transfer*, 37 (2010) 914-923.
- [78] E. Vázquez, M. Prato, Carbon Nanotubes and Microwaves: Interactions, Responses, and Applications, *ACS Nano*, 3 (2009) 3819-3824.
- [79] G. Yang, W. Choi, X. Pu, C. Yu, Scalable synthesis of bi-functional high-performance carbon nanotube sponge catalysts and electrodes with optimum C-N-Fe coordination for oxygen reduction reaction, *Energy & Environmental Science*, 8 (2015) 1799-1807.
- [80] T. Kim, J. Lee, K.-H. Lee, Microwave heating of carbon-based solid materials, *Carbon Letters*, 15 (2014) 15-24.
- [81] S. Chandrasekaran, T. Basak, R. Srinivasan, Microwave heating characteristics of graphite based powder mixtures, *International Communications in Heat and Mass Transfer*, 48 (2013) 22-27.

- [82] C. Yu, Y. Ryu, L. Yin, H. Yang, Modulating electronic transport properties of carbon nanotubes to improve the thermoelectric power factor via nanoparticle decoration, *ACS Nano*, 5 (2011) 1297-1303.
- [83] Y. Ryu, D. Freeman, C. Yu, High electrical conductivity and n-type thermopower from double-/single-wall carbon nanotubes by manipulating charge interactions between nanotubes and organic/inorganic nanomaterials, *Carbon*, 49 (2011) 4745-4751.
- [84] B.I. Kharisov, O.V. Kharissova, U. Ortiz Méndez, I.G. De La Fuente, Decoration of carbon nanotubes with metal nanoparticles: Recent trends, *Synthesis and Reactivity in Inorganic, Metal-Organic, and Nano-Metal Chemistry*, 46 (2016) 55-76.
- [85] W.G. Devine, N.E. Leadbeater, Probing the energy efficiency of microwave heating and continuous-flow conventional heating as tools for organic chemistry, *Arkivoc*, 2011 (2011) 127-143.
- [86] L.H.T. GmbH, Microwave rubber heating technology, *Linn High Therm*, 2017.
- [87] Microwave Process Engineering Research Group, Advantages of microwave process engineering, *University of Nottingham*, 2017.
- [88] K. Parvez, S. Yang, Y. Hernandez, A. Winter, A. Turchanin, X. Feng, K. Müllen, Nitrogen-doped graphene and its iron-based composite as efficient electrocatalysts for oxygen reduction reaction, *ACS Nano*, 6 (2012) 9541-9550.
- [89] L. Li, S.-H. Chai, S. Dai, A. Manthiram, Advanced hybrid Li-air batteries with high-performance mesoporous nanocatalysts, *Energy & Environmental Science*, 7 (2014) 2630-2636.

- [90] C. Erbay, X. Pu, W. Choi, M.-J. Choi, Y. Ryu, H. Hou, F. Lin, P. de Figueiredo, C. Yu, A. Han, Control of geometrical properties of carbon nanotube electrodes towards high-performance microbial fuel cells, *Journal of Power Sources*, 280 (2015) 347-354.
- [91] S. Jee, W. Choi, C.H. Ahn, G. Yang, H.K. Cho, J.-H. Lee, C. Yu, Enhanced oxygen reduction and evolution by in-situ decoration of hematite nanoparticles on carbon nanotube cathode for high-capacity nonaqueous lithium-oxygen batteries, *Journal of Materials Chemistry A*, 3 (2015) 13767-13775.
- [92] G. Yang, W. Choi, X. Pu, C. Yu, Scalable synthesis of bi-functional high-performance carbon nanotube sponge catalysts and electrodes with optimum C–N–Fe coordination for oxygen reduction reaction, *Energy & Environmental Science*, 8 (2015) 1799-1807.
- [93] V.R. Stamenkovic, B. Fowler, B.S. Mun, G. Wang, P.N. Ross, C.A. Lucas, N.M. Marković, Improved oxygen reduction activity on Pt₃Ni(111) via increased surface site availability, *Science*, 315 (2007) 493-497.
- [94] C.W.B. Bezerra, L. Zhang, K. Lee, H. Liu, A.L.B. Marques, E.P. Marques, H. Wang, J. Zhang, A review of Fe–N/C and Co–N/C catalysts for the oxygen reduction reaction, *Electrochimica Acta*, 53 (2008) 4937-4951.
- [95] B. Wang, Recent development of non-platinum catalysts for oxygen reduction reaction, *Journal of Power Sources*, 152 (2005) 1-15.
- [96] J.-S. Li, S.-L. Li, Y.-J. Tang, M. Han, Z.-H. Dai, J.-C. Bao, Y.-Q. Lan, Nitrogen-doped Fe/Fe₃C@graphitic layer/carbon nanotube hybrids derived from MOFs: efficient

bifunctional electrocatalysts for ORR and OER, *Chemical Communications*, 51 (2015) 2710-2713.

[97] X. Zhou, J. Qiao, L. Yang, J. Zhang, A review of graphene-based nanostructural materials for both catalyst supports and metal-free catalysts in PEM fuel cell oxygen reduction reactions, *Advanced Energy Materials*, 4 (2014) 1301523.

[98] E. Proietti, F. Jaouen, M. Lefèvre, N. Larouche, J. Tian, J. Herranz, J.-P. Dodelet, Iron-based cathode catalyst with enhanced power density in polymer electrolyte membrane fuel cells, *Nature Communications*, 2 (2011) 416.

[99] M. Lefèvre, E. Proietti, F. Jaouen, J.-P. Dodelet, Iron-based catalysts with improved oxygen reduction activity in polymer electrolyte fuel cells, *Science*, 324 (2009) 71-74.

[100] J. Yang, D.-J. Liu, N.N. Kariuki, L.X. Chen, Aligned carbon nanotubes with built-in FeN₄ active sites for electrocatalytic reduction of oxygen, *Chemical Communications*, (2008) 329-331.

[101] H.L. Peng, Z.Y. Mo, S.J. Liao, H.G. Liang, L.J. Yang, F. Luo, H.Y. Song, Y.L. Zhong, B.Q. Zhang, High performance Fe- and N- doped carbon catalyst with graphene structure for oxygen reduction, *Scientific Reports*, 3 (2013) 1765

[102] Y. Zhang, J. Ge, L. Wang, D. Wang, F. Ding, X. Tao, W. Chen, Manageable N-doped graphene for high performance oxygen reduction reaction, *Scientific Reports*, 3 (2013) 2771.

- [103] Y. Liang, Y. Li, H. Wang, J. Zhou, J. Wang, T. Regier, H. Dai, Co_3O_4 nanocrystals on graphene as a synergistic catalyst for oxygen reduction reaction, *Nature Materials*, 10 (2011) 780-786.
- [104] W. Choi, G. Yang, S.L. Kim, P. Liu, H.-J. Sue, C. Yu, One-step synthesis of nitrogen-iron coordinated carbon nanotube catalysts for oxygen reduction reaction, *Journal of Power Sources*, 313 (2016) 128-133.
- [105] H. Sjöström, S. Stafström, M. Boman, J.E. Sundgren, Superhard and elastic carbon nitride thin films having fullerenelike microstructure, *Physical Review Letters*, 75 (1995) 1336-1339.
- [106] M. Dresselhaus, A. Jorio, R. Saito, Characterizing graphene, graphite, and carbon nanotubes by Raman spectroscopy, *Annual Review of Condensed Matter Physics*, 1 (2010) 89-108.
- [107] Y. Ryu, L. Yin, C. Yu, Dramatic electrical conductivity improvement of carbon nanotube networks by simultaneous de-bundling and hole-doping with chlorosulfonic acid, *Journal of Materials Chemistry*, 22 (2012) 6959-6964.
- [108] S. Kundu, T.C. Nagaiah, W. Xia, Y. Wang, S.V. Dommele, J.H. Bitter, M. Santa, G. Grundmeier, M. Bron, W. Schuhmann, M. Muhler, Electrocatalytic activity and stability of nitrogen-containing carbon nanotubes in the oxygen reduction reaction, *Journal of Physical Chemistry C*, 113 (2009) 14302-14310.

- [109] S. Wang, D. Yu, L. Dai, Polyelectrolyte functionalized carbon nanotubes as efficient metal-free electrocatalysts for oxygen reduction, *Journal of the American Chemical Society*, 133 (2011) 5182-5185.
- [110] Q. He, X. Yang, X. Ren, B.E. Koel, N. Ramaswamy, S. Mukerjee, R. Kostecki, A novel CuFe-based catalyst for the oxygen reduction reaction in alkaline media, *Journal of Power Sources*, 196 (2011) 7404-7410.
- [111] K. Lee, M.S. Ahmed, S. Jeon, Electrochemical deposition of silver on manganese dioxide coated reduced graphene oxide for enhanced oxygen reduction reaction, *Journal of Power Sources*, 288 (2015) 261-269.
- [112] J. Larminie, A. Dicks, J. Larminie, A. Dicks, *Fuel Cell Systems Analysed, Fuel Cell Systems Explained*, John Wiley & Sons, Ltd., 2013, pp. 369-389.
- [113] R. Liu, D. Wu, X. Feng, K. Müllen, Nitrogen-doped ordered mesoporous graphitic arrays with high electrocatalytic activity for oxygen reduction, *Angewandte Chemie International Edition*, 49 (2010) 2565-2569.
- [114] J. Maruyama, I. Abe, Application of conventional activated carbon loaded with dispersed Pt to PEFC catalyst layer, *Electrochimica Acta*, 48 (2003) 1443-1450.
- [115] K. Niu, B. Yang, J. Cui, J. Jin, X. Fu, Q. Zhao, J. Zhang, Graphene-based non-noble-metal Co/N/C catalyst for oxygen reduction reaction in alkaline solution, *Journal of Power Sources*, 243 (2013) 65-71.

- [116] J. Pels, F. Kapteijn, J. Moulijn, Q. Zhu, K. Thomas, Evolution of nitrogen functionalities in carbonaceous materials during pyrolysis, *Carbon*, 33 (1995) 1641-1653.
- [117] E.N. Nxumalo, N.J. Coville, Nitrogen doped carbon nanotubes from organometallic compounds: A review, *Materials*, 3 (2010) 2141-2171.
- [118] R. Arrigo, M. Havecker, R. Schlogl, D.S. Su, Dynamic surface rearrangement and thermal stability of nitrogen functional groups on carbon nanotubes, *Chemical Communications*, (2008) 4891-4893.
- [119] S. Chen, J. Bi, Y. Zhao, L. Yang, C. Zhang, Y. Ma, Q. Wu, X. Wang, Z. Hu, Nitrogen-doped carbon nanocages as efficient metal-free electrocatalysts for oxygen reduction reaction, *Advanced Materials*, 24 (2012) 5593-5597.
- [120] G. Faubert, R. Côté, J. Dodelet, M. Lefevre, P. Bertrand, Oxygen reduction catalysts for polymer electrolyte fuel cells from the pyrolysis of Fe II acetate adsorbed on 3, 4, 9, 10-perylenetetracarboxylic dianhydride, *Electrochimica Acta*, 44 (1999) 2589-2603.
- [121] K. Artyushkova, B. Kiefer, B. Halevi, A. Knop-Gericke, R. Schlogl, P. Atanassov, Density functional theory calculations of XPS binding energy shift for nitrogen-containing graphene-like structures, *Chemical Communications*, 49 (2013) 2539-2541.
- [122] A.P. Grosvenor, B.A. Kobe, M.C. Biesinger, N.S. McIntyre, Investigation of multiplet splitting of Fe 2p XPS spectra and bonding in iron compounds, *Surface and Interface Analysis*, 36 (2004) 1564-1574.

- [123] T. Droubay, S.A. Chambers, Surface-sensitive Fe 2p photoemission spectra for α -Fe₂O₃(0001): The influence of symmetry and crystal-field strength, *Physical Review B*, 64 (2001) 205-414.
- [124] A.J. Bard, *Electrochemical Methods, Fundamental and Applications*, John Wiley & Sons, New York 1980.
- [125] K.E. Gubbins, R.D. Walker, The solubility and diffusivity of oxygen in electrolytic solutions, *Journal of The Electrochemical Society*, 112 (1965) 469-471.
- [126] R.E. Davis, G.L. Horvath, C.W. Tobias, The solubility and diffusion coefficient of oxygen in potassium hydroxide solutions, *Electrochimica Acta*, 12 (1967) 287-297.
- [127] Z.-S. Wu, S. Yang, Y. Sun, K. Parvez, X. Feng, K. Müllen, 3D nitrogen-doped graphene aerogel-supported Fe₃O₄ nanoparticles as efficient electrocatalysts for the oxygen reduction reaction, *Journal of the American Chemical Society*, 134 (2012) 9082-9085.
- [128] Y. Zhang, K. Fugane, T. Mori, L. Niu, J. Ye, Wet chemical synthesis of nitrogen-doped graphene towards oxygen reduction electrocatalysts without high-temperature pyrolysis, *Journal of Materials Chemistry*, 22 (2012) 6575-6580.
- [129] A.C. Pierre, G.M. Pajonk, *Chemistry of aerogels and their applications*, *Chemical Reviews*, 102 (2002) 4243-4266.
- [130] B. Yuan, S. Ding, D. Wang, G. Wang, H. Li, Heat insulation properties of silica aerogel/glass fiber composites fabricated by press forming, *Materials Letters*, 75 (2012) 204-206.

- [131] S.N. Schiffres, K.H. Kim, L. Hu, A.J.H. McGaughey, M.F. Islam, J.A. Malen, Gas diffusion, energy transport, and thermal accommodation in single-walled carbon nanotube aerogels, *Advanced Functional Materials*, 22 (2012) 5251-5258.
- [132] J.N. Lee, C. Park, G.M. Whitesides, Solvent compatibility of poly(dimethylsiloxane)-based microfluidic devices, *Analytical Chemistry*, 75 (2003) 6544-6554.
- [133] J. Hone, M. Llaguno, N. Nemes, A. Johnson, J. Fischer, D. Walters, M. Casavant, J. Schmidt, R. Smalley, Electrical and thermal transport properties of magnetically aligned single wall carbon nanotube films, *Applied Physics Letters*, 77 (2000) 666-668.
- [134] P. Kim, L. Shi, A. Majumdar, P. McEuen, Thermal transport measurements of individual multiwalled nanotubes, *Physical Review Letters*, 87 (2001) 215502.
- [135] Q. Zhang, G. Chen, S. Yoon, J. Ahn, S. Wang, Q. Zhou, Q. Wang, J. Li, Thermal conductivity of multiwalled carbon nanotubes, *Physical Review B*, 66 (2002) 165440.
- [136] J. Hong, J. Lee, C.K. Hong, S.E. Shim, Effect of dispersion state of carbon nanotube on the thermal conductivity of poly(dimethyl siloxane) composites, *Current Applied Physics*, 10 (2010) 359-363.
- [137] S.Y. Kwon, I.M. Kwon, Y.-G. Kim, S. Lee, Y.-S. Seo, A large increase in the thermal conductivity of carbon nanotube/polymer composites produced by percolation phenomena, *Carbon*, 55 (2013) 285-290.

- [138] C. Wang, T. Chen, S. Chang, S. Cheng, T. Chin, Strong carbon-nanotube–polymer bonding by microwave irradiation, *Advanced Functional Materials*, 17 (2007) 1979-1983.
- [139] Y. Si, J. Yu, X. Tang, J. Ge, B. Ding, Ultralight nanofibre-assembled cellular aerogels with superelasticity and multifunctionality, *Nature Communications*, 5 (2014).
- [140] M. Nour, K. Berean, S. Balendhran, J.Z. Ou, J. Du Plessis, C. McSweeney, M. Bhaskaran, S. Sriram, K. Kalantar-zadeh, CNT/PDMS composite membranes for H₂ and CH₄ gas separation, *International Journal of Hydrogen Energy*, 38 (2013) 10494-10501.
- [141] S.K. Yadav, I.J. Kim, H.J. Kim, J. Kim, S.M. Hong, C.M. Koo, PDMS/MWCNT nanocomposite actuators using silicone functionalized multiwalled carbon nanotubes via nitrene chemistry, *Journal of Materials Chemistry C*, 1 (2013) 5463-5470.
- [142] T. Wu, B. Chen, Synthesis of multiwalled carbon nanotube-reinforced polyborosiloxane nanocomposites with mechanically adaptive and self-healing capabilities for flexible conductors, *ACS Applied Materials & Interfaces*, 8 (2016) 24071-24078.
- [143] Y. Li, L.a. Fernandez-Recio, P. Gerstel, V. Srot, P.A.v. Aken, G. Kaiser, M. Burghard, J. Bill, Chemical modification of single-walled carbon nanotubes for the reinforcement of precursor-derived ceramics, *Chemistry of Materials*, 20 (2008) 5593-5599.

- [144] M. Shahzad, M. Giorcelli, N. Shahzad, S. Guastella, M. Castellino, P. Jagdale, A. Tagliaferro, Study of carbon nanotubes based polydimethylsiloxane composite films, *Journal of Physics: Conference Series*, IOP Publishing, 2013, pp. 012010.
- [145] M.A. Pantoja-Castro, J.F. Pérez-Robles, H. González-Rodríguez, Y. Vorobiev-Vasilievitch, H.V. Martínez-Tejada, C. Velasco-Santos, Synthesis and investigation of PMMA films with homogeneously dispersed multiwalled carbon nanotubes, *Materials Chemistry and Physics*, 140 (2013) 458-464.
- [146] C. McClory, T. McNally, M. Baxendale, P. Pötschke, W. Blau, M. Ruether, Electrical and rheological percolation of PMMA/MWCNT nanocomposites as a function of CNT geometry and functionality, *European Polymer Journal*, 46 (2010) 854-868.
- [147] J. Sandler, M.S.P. Shaffer, A.H. Windle, M.P. Halsall, M.A. Montes-Morán, C.A. Cooper, R.J. Young, Variations in the Raman peak shift as a function of hydrostatic pressure for various carbon nanostructures: A simple geometric effect, *Physical Review B*, 67 (2003) 035417.
- [148] J.R. Wood, M.D. Frogley, E.R. Meurs, A.D. Prins, T. Peijs, D.J. Dunstan, H.D. Wagner, Mechanical response of carbon nanotubes under molecular and macroscopic pressures, *The Journal of Physical Chemistry B*, 103 (1999) 10388-10392.
- [149] H. Sun, Z. Xu, C. Gao, Multifunctional, Ultra-flyweight, synergistically assembled carbon aerogels, *Advanced Materials*, 25 (2013) 2554-2560.

- [150] J. Zou, J. Liu, A.S. Karakoti, A. Kumar, D. Joung, Q. Li, S.I. Khondaker, S. Seal, L. Zhai, Ultralight multiwalled carbon nanotube aerogel, *ACS Nano*, 4 (2010) 7293-7302.
- [151] B. Wicklein, A. Kocjan, G. Salazar-Alvarez, F. Carosio, G. Camino, M. Antonietti, L. Bergström, Thermally insulating and fire-retardant lightweight anisotropic foams based on nanocellulose and graphene oxide, *Nature Nanotechnology*, 10 (2015) 277-283.
- [152] M.A.B. Meador, A.S. Weber, A. Hindi, M. Naumenko, L. McCorkle, D. Quade, S.L. Vivod, G.L. Gould, S. White, K. Deshpande, Structure–property relationships in porous 3D nanostructures: Epoxy-cross-linked silica aerogels produced using ethanol as the solvent, *ACS Applied Materials & Interfaces*, 1 (2009) 894-906.
- [153] E.M. Arndt, M.D. Gawryla, D.A. Schiraldi, Elastic, low density epoxy/clay aerogel composites, *Journal of Materials Chemistry*, 17 (2007) 3525-3529.
- [154] C. Wu, X. Huang, X. Wu, R. Qian, P. Jiang, Mechanically flexible and multifunctional polymer-based graphene foams for elastic conductors and oil-water separators, *Advanced Materials*, 25 (2013) 5658-5662.
- [155] H. Hu, Z. Zhao, W. Wan, Y. Gogotsi, J. Qiu, Ultralight and highly compressible graphene aerogels, *Advanced Materials*, 25 (2013) 2219-2223.
- [156] L. Qiu, J.Z. Liu, S.L.Y. Chang, Y. Wu, D. Li, Biomimetic superelastic graphene-based cellular monoliths, *Nature Communications*, 3 (2012) 1241.

- [157] K.H. Kim, Y. Oh, M.F. Islam, Graphene coating makes carbon nanotube aerogels superelastic and resistant to fatigue, *Nature Nanotechnology*, 7 (2012) 562-566.
- [158] R. Baetens, B.P. Jelle, A. Gustavsen, Aerogel insulation for building applications: a state-of-the-art review, *Energy and Buildings*, 43 (2011) 761-769.
- [159] X. Lu, M. Arduini-Schuster, Thermal conductivity of monolithic organic aerogels, *Science*, 255 (1992) 971.
- [160] S.T. Huxtable, D.G. Cahill, S. Shenogin, L. Xue, R. Ozisik, P. Barone, M. Usrey, M.S. Strano, G. Siddons, M. Shim, P. Keblinski, Interfacial heat flow in carbon nanotube suspensions, *Nature Materials*, 2 (2003) 731-734.
- [161] K. Bui, B.P. Grady, D.V. Papavassiliou, Heat transfer in high volume fraction CNT nanocomposites: Effects of inter-nanotube thermal resistance, *Chemical Physics Letters*, 508 (2011) 248-251.
- [162] E.W. Lemmon, R.T. Jacobsen, Viscosity and thermal conductivity equations for nitrogen, oxygen, argon, and air, *International Journal of Thermophysics*, 25 (2004) 21-69.
- [163] K. Sobolev, Nanotechnology and nanoengineering of construction materials, in: K. Sobolev, S.P. Shah (Eds.) *Nanotechnology in Construction: Proceedings of NICOM5*, Springer International Publishing, Cham, 2015, pp. 3-13.
- [164] D.J. Yang, Q. Zhang, G. Chen, S.F. Yoon, J. Ahn, S.G. Wang, Q. Zhou, Q. Wang, J.Q. Li, Thermal conductivity of multiwalled carbon nanotubes, *Physical Review B*, 66 (2002) 165440.

[165] Z. Han, A. Fina, Thermal conductivity of carbon nanotubes and their polymer nanocomposites: A review, *Progress in Polymer Science*, 36 (2011) 914-944.